Engineering Structures 345 (2025) 121462

Contents lists available at ScienceDirect

Engineering Structures

journal homepage: www.elsevier.com/locate/engstruct

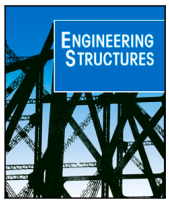

An equivalent shell model for elastic gridshell analysis

Giambattista Romano [a], Salvatore Sessa [a,*], Daniele Lancia [b], Luciano Rosati [a]

[a] Department of Structures for Engineering and Architecture, University of Naples Federico II, Via Claudio, 21, 80124, Napoli, Italy
[b] Department of Architecture, University of Naples Federico II, Via Forno Vecchio, 36, 80134, Napoli, Italy

ARTICLE INFO

Keywords:
Gridshells
Equivalent continuum model
Homogenization
Active bending
Finite element analysis

ABSTRACT

This study presents a novel framework for modelling elastic gridshells, and particularly their deployment phase, using a continuum shell model derived from the Special Cosserat Theory of rods. Such an approach enforces energetic equivalence between discrete rod-based gridshell configurations and a continuum shell representation, enabling the derivation of constitutive parameters that accurately reflect the structural behaviour. Numerical simulations validate the model's remarkable accuracy, achieving a maximum percentage root mean square error of about 2% when compared to traditional discrete beam models. Experimental validation on a real-world structure, the Toledo 2.0 gridshell, further confirms the model's predictive capability. The proposed methodology provides an efficient and versatile tool for the early stages of gridshell design. It permits rapid assessment of structural performance, thus significantly reducing computational overhead while maintaining high accuracy.

1. Introduction

Gridshells represent sophisticated structural solutions characterized by planar grids that are driven in three-dimensional configuration by taking advantage of geometrical nonlinearity through controlled deformative processes [1–3].

Although efficient computational tools addressing the analyses of active-bending beam structure are available in the literature [4–6], strategies of structural homogenization have been investigated since the second half of the 20th century. Such approaches aim to replace the original model, made of a discrete grid of rods, with a continuum shell [7].

The definition of an equivalent continuum was initially exploited in order to avoid design errors originated by the inability of estimating structural safety factors during the initial phases of the architectural conception. Such an issue is still essential nowadays: indeed, the active bending process is intrinsically lacking of solution uniqueness and presents several load–displacement path bifurcations [8,9]. Hence, the geometrical design process turns out to be particularly complex because, once a *target shape* of the gridshell has been conceived, it is necessary to determine a combination of both undeformed geometry and mechanical properties as well as the active bending process leading to the desired deformed configuration [10]. In addition, an estimate of some safety factor with respect to working loads, although approximate, is essential for preventing that, after a complex geometric design, the structure does not fulfil the structural capacity checks [11]. As a matter of fact, the whole design procedure can be interpreted as a complex optimization problem involving an objective function (some sort of gap with respect to a *target shape*), one or more constraints (enforcing the fulfilment of performance requirements and/or capacity checks) and a set of design parameters [12]. These consist of geometrical features (e.g. the undeformed shape), active bending paths, and mechanical properties (i.e. spacing, direction, stiffness, and inertia of beams). Indeed, the use of discrete beam models for addressing such problems is difficult and burdensome while the use of an equivalent continuum model is essentially preferable for many reasons [13,14]. First, continuum models usually involve a significantly lower number of degrees of freedom than discrete models. Moreover, a modification of properties, such as beam spacing or orientation, results in the modification of the whole discrete beam model, while it induces a mere modification of some constitutive parameters of the equivalent continuum model [15]. Additionally, the chance of having a parameterized model opens further possibilities of using very effective optimization strategies, such as those involving direct differentiation procedures of the target outcomes.

Beyond the evident computational advantages, one of the most remarkable strengths of homogenized continuum models lies in their amenability to analytical solutions in a variety of settings. Unlike purely numerical approaches, analytical solutions provide profound insight

* Corresponding author.
E-mail addresses: giambattista.romano@unina.it (G. Romano), salvatore.sessa2@unina.it (S. Sessa), daniele.lancia@unina.it (D. Lancia), rosati@unina.it (L. Rosati).

https://doi.org/10.1016/j.engstruct.2025.121462
Received 24 April 2025; Received in revised form 4 September 2025; Accepted 24 September 2025
Available online 30 September 2025

into the underlying deformation mechanisms, enabling a theoretical understanding of the structural behaviour of morphing lattices. They may offer powerful tools to investigate how geometric and mechanical parameters can influence pivotal phenomena such as deformation modes and bifurcation patterns, thus enriching the interpretation of structural responses beyond the possibilities of standard numerical simulations.

Moreover, in the case of morphogenetic procedures for form-finding purposes, homogenized models permit an easy computation of the generalized forces. In this sense, the contribution of the local geometric and mechanical properties of the rods to the global stiffness become evident thus fostering useful information for structural design.

Within this context, different approaches for the characterization of the equivalent continuum models have been proposed. The Equivalent Stiffness Method [7] provides an equivalent thickness and homogenized stiffness parameter as functions of the beam properties, although it is focused on the membrane behaviour. Nevertheless, being such a continuum essentially isotropic, this approach turns out to be not sufficiently accurate. The Split Rigidity Method [16] introduces flexure while the Orthotropic Equivalent Continuum Method [17–19] accounts for anisotropies. Moreover, while such procedures aim to calibrate a continuum model matching the discrete one, the inverse path has been followed by Regalo et al. [20] for design purposes.

As a matter of fact, the Orthotropic Equivalent Continuum strategy presents some drawbacks that limits its accuracy and applicability. As a first consideration, the method is developed in the case of gridshells with orthogonal rods, whose directions are coincident with the mechanical reference system. Hence, its generalization to the case of non-orthogonal rods is not straightforward. A further aspect concerns the continuum kinematics. In fact, equivalence is commonly enforced by considering a reference area element corresponding to a single cell of the discrete grid. Such an element is therefore deformed by each single strain component typical of the Cauchy continuum so that a stiffness equivalence can be enforced. Nevertheless, because of the peculiar topology of gridshells, the traditional strain components are not exhaustive of the gridshell kinematics [21,22].

Such drawbacks are partially addressed by the Kirchhoff–Love type shell framework for rigid gridshells [23,24] that combines homogenization with optimization strategies for mapping two-way grids on free-form surfaces and for their structural optimization, thus showing homogenization capabilities in inverse problems and form design. Moreover, enhanced plate models [25,26] extend the Reissner–Mindlin and Bending-Gradient approaches to beam lattices, providing an energy-consistent framework to determine effective shear stiffness.

Although highly relevant to gridshell analysis, such approaches remain within a Cauchy continuum framework and are not capable of capturing generalized motions, such as drill modes, that are intrinsic to Cosserat media.

In order to overcome such drawbacks, aim of this work is to formulate a strategy for the characterization of a continuum constitutive model that is energetically equivalent to a coarse gridshell.

Building on previous models for pantographic structures [27–29], we formulate an approach for modelling gridshells having rod bundles with arbitrary orientation.

In particular, a discrete model is formulated in Section 2.1 by specializing the Special Cosserat Theory of rods. Subsequently, the continuum model is formulated in Section 2.2 by introducing a local reference system consistently with the geometric parameters of the discrete model. This permits, in Section 2.3, to describe the kinematics of both models by means of similar variables so that the constitutive parameters of the continuum can be computed by enforcing equality between the elastic energy of both models. Although the equivalence is firstly derived for gridshells with orthogonal rods, it is generalized to the case of non-orthogonal bundles in Section 2.4.

The presented strategy is then validated from the numerical point of view. In particular, the elastic energy functional determined in Section 2.3 has been used to implement Finite Element continuum model

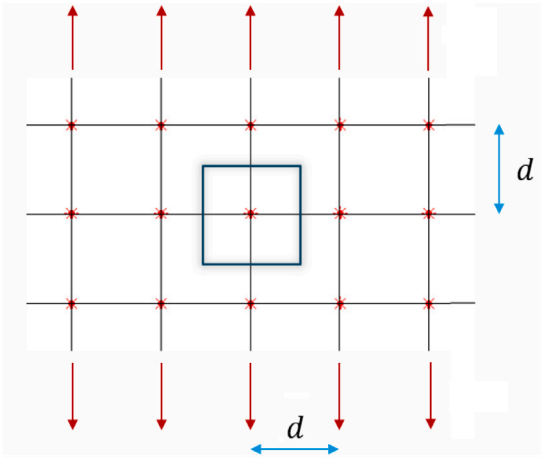

Fig. 1. Equivalent area element for an equally spaced grid of rods.

in *Comsol Multiphysics*® [30]. The response of the continuum model has been compared with those of discrete models having the same geometry and modelled in *MARC*® *Mentat*® [31]. Such a comparison involved purely numerical tests, shown in Section 3 and exploiting both in-plane and out-of-plane deformative processes. Numerical tests aiming at a mesh sensitivity analysis are reported in Section 3.4.

In order to investigate the effectiveness and accuracy of the proposed strategy, an experimental assessment is presented in Section 4 where a real case-study, the *Toledo 2.0* gridshell presented in [32], has been analysed in order to compare the response of the equivalent continuum model with a real structure.

Both the numerical tests and the experimental assessment have shown an excellent accuracy of the proposed model. In particular, the continuum model provides a flexible framework for rapid structural configuration analysis, mitigating the computational overhead associated with repeated topological modifications of the discrete models typical of the early-stage design phases. Conversely, the continuum model suffers from a greater difficulty in evaluating detailed stress characteristics like axial forces, shear forces, and bending moments.

It is worth being emphasized that the scope of the present work is specifically restricted to the deployment of elastic gridshells, i.e. before that bracing systems are assembled, for form-finding purposes.

In particular, during the gridshell deployment phase, drill and shear modes are required to be free in order to achieve double curvature of the final shape. In such a case, the difference between a Cosserat and a classical Cauchy continuum is essential, being the latter one not exhaustive of the required kinematics, while it is marginal in presence of stiffening devices that restrain drilling and shear deformation modes. Additionally, during the deployment phase, the determination of internal actions can afford some approximation since external loads are not introduced yet. Hence, the proposed formulation is particularly suited for investigating gridshells during their morphogenetic process, before the introduction of any stabilizing system.

2. Definition of the two-dimensional equivalent model

Gridshells are usually made of, at least, two sets of parallel rods belonging to the horizontal plane in their undeformed configuration. Their connections consist of planar hinges so that rotations about the axis orthogonal to the plane tangent to both elements is unconstrained.

Although orthogonal beam sets are often encountered in practice, there is also a rich tradition of non-orthogonal configurations. In particular, Chebychev nets have been widely used in elastic gridshell design, starting from Frei Otto's pioneering work, and are discussed extensively in Schober's monograph on gridshells. Mechanical models

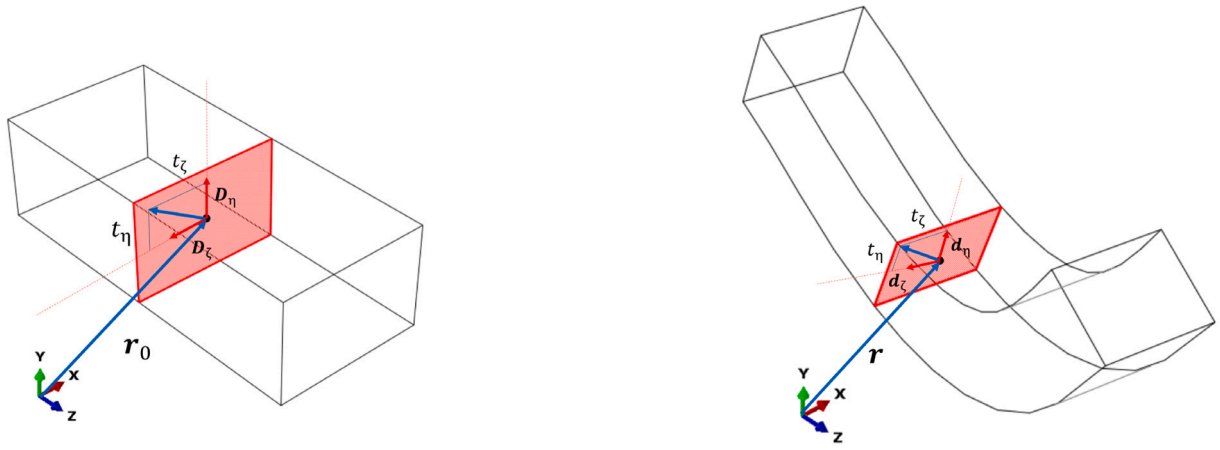

(a) Reference (Undeformed) configuration; (b) Current (Deformed) configuration;

Fig. 2. Rods local reference systems.

of Chebychev nets have also been proposed, often borrowing from fabric mechanics [33,34]. Hence, the orthogonal assumption does not exhaust the spectrum of gridshell topologies.

An effective strategy for the definition of the two-dimensional continuum model consists in exploiting the *Hill–Mandel lemma*, or *Energy Equivalence Principle*, by enforcing energetic equivalence between a continuum model and a discrete one consisting of a parameterized set of rods [20,35]. Such a condition is formulated with respect to an equivalent area element that represents the neighbourhood of a generic point of the gridshell.

For simplicity, we initially refer to a gridshell with two orthogonal sets of rods, although the homogenized model will be extended to the case of arbitrary orientations in Section 2.4. In case of orthogonal rods, the equivalent area element, represented in Fig. 1, can be defined by a characteristic dimension d assumed to be equal to the rods spacing. Hence, the equivalent area element is defined as a rectangular neighbourhood of the connecting node with length sides equal to the grid spacing.

2.1. Discrete rod model

The behaviour of the discretized elements can be defined by Kirchhoff rods, a particularization of the Special Cosserat theory of rods [36].

Within this theoretical framework, a beam in its reference (undeformed) configuration can be described as

$$\boldsymbol{\xi}_0(s, t_\zeta, t_\eta) = \mathbf{r}_0(s) + t_\zeta \mathbf{D}_\zeta(s) + t_\eta \mathbf{D}_\eta \tag{1}$$

where $\{\mathbf{D}_\zeta, \mathbf{D}_\eta, \mathbf{r}_0'\}$ is an orthonormal reference frame, t_ζ and t_η are the coordinates of a generic point on a cross section located at the curvilinear abscissa $s \in (0, L)$, as shown in Fig. 2(a), and $\mathbf{r}_0$ denotes a generic point of the undeformed configuration of the beam axis. The prime denotes the derivative with respect to s.

Similarly, the deformed configuration of the beam can be described as:

$$\boldsymbol{\xi}(s, t_\zeta, t_\eta) = \mathbf{r}(s) + t_\zeta \mathbf{d}_\zeta(s) + t_\eta \mathbf{d}_\eta(s) \tag{2}$$

where $\mathbf{r}(s)$ denotes a generic point of the deformed configuration of the beam axis and $\{\mathbf{d}_\zeta(s), \mathbf{d}_\eta(s)\}$ are two orthogonal unit vectors, obtained through a rigid rotation of the unit vectors $\{\mathbf{D}_\zeta(s), \mathbf{D}_\eta(s)\}$, as shown in Fig. 2(b).

The three unit vectors $\{\mathbf{r}', \mathbf{d}_\zeta, \mathbf{d}_\eta\}$ are used in order to characterize the gridshell kinematics. We assume the following strain measures for the beam:

1. Hencky Elongation: $\epsilon = \ln(|\mathbf{r}'(s)|)$;

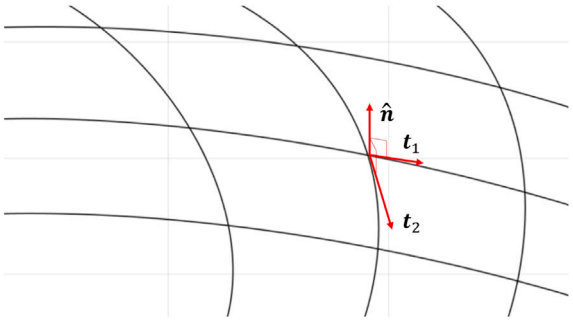

Fig. 3. Vectors tangent to the deformed configuration.

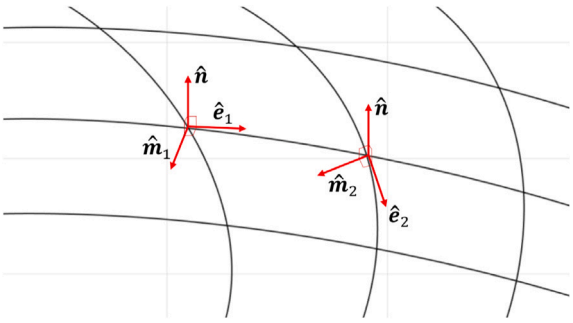

Fig. 4. Local reference frames.

2. Bending curvature about $\mathbf{d}_\zeta$:
   $\kappa_\zeta = \mathbf{d}_\eta'(s) \cdot \mathbf{d}_\theta(s) = -\mathbf{d}_\eta(s) \cdot \mathbf{d}_\theta'(s)$;
3. Bending curvature about $\mathbf{d}_\eta$:
   $\kappa_\eta = \mathbf{d}_\zeta(s) \cdot \mathbf{d}_\theta'(s) = -\mathbf{d}_\zeta'(s) \cdot \mathbf{d}_\theta(s)$;
4. Torsional curvature:
   $\tau = \mathbf{d}_\zeta'(s) \cdot \mathbf{d}_\eta(s) = -\mathbf{d}_\zeta(s) \cdot \mathbf{d}_\eta'(s)$;

where $\mathbf{d}_\theta(s) = \mathbf{d}_\zeta(s) \times \mathbf{d}_\eta(s)$.

According to the Kirchhoff rods model, the elastic energy W_b can be defined as a quadratic form of the beam strain components, thus assuming that the material has a linear-elastic behaviour. Specifically, the elastic energy turns out to be:

$$W_b = \int_L \frac{1}{2} \left(EA\epsilon^2 + EI_\zeta \kappa_\zeta{}^2 + EI_\eta \kappa_\eta{}^2 + GJ\tau^2 \right) dL \tag{3}$$

where E denotes the Young's modulus of the material, G is the second Lamé constant, A is the cross section area of each rod, I_ζ and I_η are the moments of inertia of the cross section with respect to $\mathbf{D}_\zeta$ and $\mathbf{D}_\eta$ and J is the relevant polar moment of inertia.

2.2. Two-dimensional model

The two-dimensional continuum is defined in a three-dimensional reference frame $\{O, \mathbf{E}_1, \mathbf{E}_2, \mathbf{E}_3\}$ with $\mathbf{E}_3$ orthogonal to the reference plane, while $\mathbf{E}_1$ and $\mathbf{E}_2$ are two orthogonal unit vectors assumed to coincide with the direction of the two families of beams if they are orthogonal.

The kinematics of the two-dimensional continuum is defined by means of its displacement field and relevant derivatives. In particular, denoting by $\mathbf{R}$ the position vector of a generic point of the two-dimensional continuum in its reference (plane) configuration, the deformed configuration can be expressed by the placement vector $\mathbf{r}$ defined as

$$\mathbf{r}(x, y) = \mathbf{R}(x, y) + \mathbf{u}(x, y) \tag{4}$$

that is

$$\mathbf{r}(x, y) = x\mathbf{E}_1 + y\mathbf{E}_2 + u_x(x, y)\mathbf{E}_1 + u_y(x, y)\mathbf{E}_2 + u_z(x, y)\mathbf{E}_3. \tag{5}$$

In order to define the strain measure, we compute two vectors, $\mathbf{t}_1$ and $\mathbf{t}_2$ tangent to the deformed configuration (see, e.g., Fig. 3) as:

$$\mathbf{t}_1 = \frac{\partial \mathbf{r}}{\partial x},\ \mathbf{t}_2 = \frac{\partial \mathbf{r}}{\partial y} \tag{6}$$

so that, within a context of large deformations, the deformation measures describing the elongation of a neighbourhood of the considered point along $\mathbf{E}_1$ and $\mathbf{E}_2$ can be defined by a logarithmic Hencky strain as:

$$\epsilon_1 = \ln\left(|\mathbf{t}_1|\right),\ \epsilon_2 = \ln\left(|\mathbf{t}_2|\right). \tag{7}$$

It is worth being emphasized that such components are equivalent to the derivative of the relevant vector $\mathbf{r}\,(s)$ in Eq. (2), since $\mathbf{E}_1$ and $\mathbf{E}_2$ have been aligned with the rods.

In order to define bending and torsion strain measures, it is necessary to determine a local reference system. Enforcing the Kirchhoff–Love hypothesis, we assume that the first unit vector of such a system is normal to the plane tangent to the deformed configuration, that is

$$\hat{\mathbf{n}} = \hat{\mathbf{e}}_1 \times \hat{\mathbf{e}}_2 \tag{8}$$

where

$$\hat{\mathbf{e}}_1 = \frac{\mathbf{t}_1}{|\mathbf{t}_1|},\ \hat{\mathbf{e}}_2 = \frac{\mathbf{t}_2}{|\mathbf{t}_2|}. \tag{9}$$

Moreover, to complete the local reference system, it is necessary to define two further unit vectors belonging to the tangent hyperplane. To this end, it is convenient to adopt the unit vectors associated with the curvature of the gridshell rods, so that the equivalence becomes straightforward. In particular, vectors $\mathbf{e}_1$, $\mathbf{e}_2$ and $\hat{\mathbf{n}}$ already represent the base of a local reference system. Nevertheless, the relevant shell curvatures cannot be easily related to the analogous quantities of the discrete model of Section 2.1. On the contrary, the unit vector normal to both, $\hat{\mathbf{e}}_1$ and $\hat{\mathbf{n}}$ defines the axis relevant to the curvature of the rods oriented along $\hat{\mathbf{e}}_1$. Hence, two unit vectors that can conveniently represent the shell curvature components are:

$$\hat{\mathbf{m}}_1 = \hat{\mathbf{n}} \times \hat{\mathbf{e}}_1,\ \hat{\mathbf{m}}_2 = \hat{\mathbf{n}} \times \hat{\mathbf{e}}_2 \tag{10}$$

and are reported in Fig. 4.

In this way, the two local reference frames $\left\{\hat{\mathbf{e}}_1, \hat{\mathbf{m}}_1, \hat{\mathbf{n}}_1\right\}$ and $\left\{\hat{\mathbf{e}}_2, \hat{\mathbf{m}}_2, \hat{\mathbf{n}}_2\right\}$ are used to define the strain measures, as done for the single beam with the local reference frame $\left\{\mathbf{r}', \mathbf{d}_\zeta, \mathbf{d}_\eta\right\}$. Therefore the bending and torsional curvatures are defined as:

$$\kappa_{12} = \frac{\partial \hat{\mathbf{e}}_1}{\partial x} \cdot \hat{\mathbf{m}}_1 \qquad \kappa_{13} = \frac{\partial \hat{\mathbf{n}}}{\partial x} \cdot \hat{\mathbf{e}}_1 \tag{11}$$

$$\kappa_{21} = \frac{\partial \hat{\mathbf{e}}_2}{\partial y} \cdot \hat{\mathbf{m}}_2 \qquad \kappa_{23} = \frac{\partial \hat{\mathbf{n}}}{\partial y} \cdot \hat{\mathbf{e}}_2$$

$$\tau_1 = \frac{\partial \hat{\mathbf{m}}_1}{\partial x} \cdot \hat{\mathbf{n}} \qquad \tau_2 = \frac{\partial \hat{\mathbf{m}}_2}{\partial y} \cdot \hat{\mathbf{n}} \tag{12}$$

where κ_{ij} is the bending curvature of the beams along i-direction in the ij-plane and τ_i is the torsional curvature of the beams along i-direction.

A picture of the generalized strain components is reported in Fig. 5 where the deformed shapes of the neighbourhood belonging to a generic point of the continuum are reported. Axes i and j belong to the continuum surface. Generalized strain component κ_{ij} induces in-plane deformation associated with drilling; hence, it is typical of the Cosserat continuum and cannot be reproduced in classical Cauchy formulations. Moreover, the traditional shear in-plane shear component γ_{ij} has been shown since it is included within the shell kinematics despite of the fact that it does not induce any energetic contribution.

In conclusion, the elastic energy W of the two-dimensional model, defined as a quadratic form of the strain measures, can be written as:

$$W = \frac{1}{2}\int_A k_e(\epsilon_1^2 + \epsilon_2^2) + k_{bp}(\kappa_{12}^2 + \kappa_{21}^2) + \\ + k_{bf}(\kappa_{13}^2 + \kappa_{23}^2) + k_t(\tau_1^2 + \tau_2^2)\, dA \tag{13}$$

where k_e and k_t are the extensional and torsional equivalent stiffness coefficients, respectively; k_{bp} and k_{bf} are the equivalent bending stiffness coefficients of the in-plane beams' flexure and out-of-plane beams' flexure, respectively. We assume equal stiffness coefficients relevant to the behaviour along $\mathbf{E}_1$ and $\mathbf{E}_2$.

It is worth being emphasized that, while strain measure ϵ_1, ϵ_2, κ_{13}, κ_{23}, τ_1 and τ_2 are traditionally adopted for shells and their physical interpretation is straightforward, curvatures κ_{12} and κ_{21} represent deformation modes relevant to in-plane bending of each family of rods. A further consideration concerns the absence of shell in-plane shear strain measure within the energy analytical form. Such a contribution does not arise because of the peculiar behaviour of the gridshell for which in-plane shear is a zero-energy rigid mechanism.

The derivatives of the elastic energy with respect to the strain measures give the internal stresses of the shell. They are represented by two forces per unit length, two in-plane bending moments per unit length, two out-of-plane bending moments per unit length and two torques per unit length, relevant to the first and second set of beams, respectively:

$$\begin{array}{cccc} \mathcal{N}_1 = \dfrac{\partial W}{\partial \epsilon_1} & \mathcal{N}_2 = \dfrac{\partial W}{\partial \epsilon_2} & \mathcal{T}_1 = \dfrac{\partial W}{\partial \tau_1} & \mathcal{T}_2 = \dfrac{\partial W}{\partial \tau_2} \\ \mathcal{M}_{12} = \dfrac{\partial W}{\partial \kappa_{12}} & \mathcal{M}_{13} = \dfrac{\partial W}{\partial \kappa_{13}} & \mathcal{M}_{21} = \dfrac{\partial W}{\partial \kappa_{21}} & \mathcal{M}_{23} = \dfrac{\partial W}{\partial \kappa_{23}} \end{array}. \tag{14}$$

It is worth being emphasized that the proposed energy formulation does not include possible mixed couplings between different components of the generalized stress. As highlighted in [37], gridshells typically exhibit an interaction between the rod torsional moment and the axial force acting in the incident elements. Such a phenomenon arises because, for constructional purposes, the rods registers are not arranged within the same plane but rather form two superposed layers. Hence, at each node, the variation of axial force occurring in a rod results in a shear force applied to the crossing rod that, in turn, induces torsion because of the eccentricity.

In the present model, such a coupling is neglected since a proper extension of the analytical framework requires the introduction of a coupling term between ϵ_i and τ_j and a far more complex description of the statics and kinematics of the model.

Being the paper mainly focused on the gridshell morphogenetic process, such a coupling can be neglected. In this respect, Section 3.5 will present an estimate of such an induced parasite torque showing that it is negligible compared to the torsional moment acting in rods.

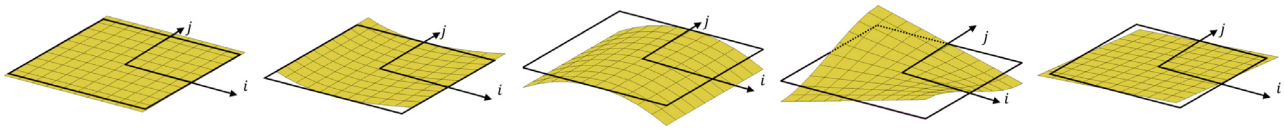

(a) Component ϵ_j; (b) Component κ_{ij}; (c) Component κ_{i3}; (d) Component τ_i; (e) Component γ_{ij};

Fig. 5. Scheme of the generalized strain components of the homogenized continuum. Undeformed shape in solid black line.

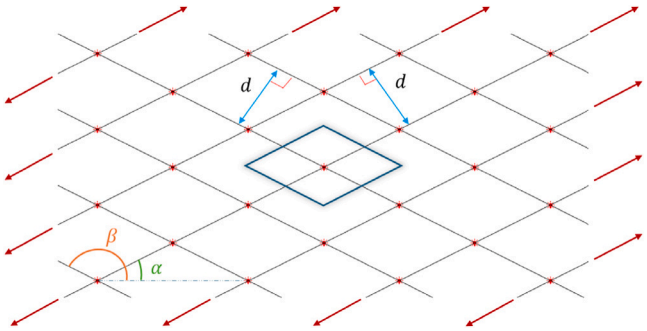

Fig. 6. Equivalent area element for an equally spaced grid of non-orthogonal rods.

2.3. Energetic equivalence

In order to determine the stiffness parameters of the equivalent shell model as a function of the gridshell characteristic properties (i.e., Young's modulus, cross-sectional area, moments of inertia), we enforce an energetic equivalence between the models defined in the previous sections. In particular, accounting for Eqs. (3) and (13) the energetic equivalence defined with respect to the equivalent area element yields:

$$W = W_{b1} + W_{b2} \tag{15}$$

where W_{b1} and W_{b2} are the elastic energy of the beams having length d and directed along $\mathbf{E}_1$ and $\mathbf{E}_2$, respectively.

The shell stiffness coefficients can be determined by observing that the energetic equivalence of Eq. (15) must be fulfilled for any arbitrary set of values of strain measures, as long as those relevant to the equivalent shell are consistent with the strains of the discrete model.

Since the shell strain components have been defined to coincide with those of the discrete system, it is possible to determine each stiffness coefficient by assuming that all strain components, but the one relevant to the coefficient to be determined, are zero.

To fix the ideas, if elongation along $\mathbf{E}_2$ is the sole non-zero strain component, Eq. (15), written for the reference area element shown in Fig. 1, becomes:

$$\frac{1}{2}\int_L EA\epsilon_2^2\, dL = \frac{1}{2}\int_A k_e\epsilon_2^2\, dA \tag{16}$$

so that:

$$k_e = \frac{EA}{d}. \tag{17}$$

Analogously, the remaining stiffness parameters turns out to be:

$$k_{bp} = \frac{EI_p}{d} \quad k_{bf} = \frac{EI_f}{d} \quad k_t = \frac{GJ}{d} \tag{18}$$

where I_p and I_f are the beam moment of inertia relevant to the in-plane and out-of-plane bending behaviour. J is the polar moment of inertia.

2.4. General disposition of rods

The equivalent continuum model can be generalized to the case of gridshells presenting non-orthogonal sets of rods. To this end, we introduce two rod orientations, $\hat{\mathbf{v}}_1$ and $\hat{\mathbf{v}}_2$, defined in the three-dimensional reference frame $\{O, \mathbf{E}_1, \mathbf{E}_2, \mathbf{E}_3\}$ as:

$$\begin{aligned}\hat{\mathbf{v}}_1 &= \cos(\alpha)\mathbf{E}_1 + \sin(\alpha)\mathbf{E}_2\\ \hat{\mathbf{v}}_2 &= \cos(\beta)\mathbf{E}_1 + \sin(\beta)\mathbf{E}_2\end{aligned} \tag{19}$$

where α and β are two arbitrary angles defining the directions of the two rods family. Adopting the subscript α and β to denote the quantities relevant to directions $\hat{\mathbf{v}}_1$ and $\hat{\mathbf{v}}_2$, respectively, it is possible to generalize the analytical energetic equivalence of Eq. (15). In fact, we can define two unit vectors analogous to $\hat{\mathbf{e}}_1$ and $\hat{\mathbf{e}}_2$ as:

$$\begin{aligned}\mathbf{t}_\alpha &= \frac{\partial \mathbf{r}}{\partial \hat{\mathbf{v}}_1} = [\nabla \mathbf{r}]\ \hat{\mathbf{v}}_1 \quad & \mathbf{t}_\beta &= \frac{\partial \mathbf{r}}{\partial \hat{\mathbf{v}}_2} = [\nabla \mathbf{r}]\ \hat{\mathbf{v}}_2\\ \hat{\mathbf{e}}_\alpha &= \frac{\mathbf{t}_\alpha}{|\mathbf{t}_\alpha|} & \hat{\mathbf{e}}_\beta &= \frac{\mathbf{t}_\beta}{|\mathbf{t}_\beta|}\end{aligned} \tag{20}$$

so that the unit vector normal to the tangent plane is:

$$\hat{\mathbf{n}} = \hat{\mathbf{e}}_\alpha \times \hat{\mathbf{e}}_\beta \tag{21}$$

and the unit vectors for computing curvatures are:

$$\hat{\mathbf{m}}_\alpha = \hat{\mathbf{n}} \times \hat{\mathbf{e}}_\alpha \quad \hat{\mathbf{m}}_\beta = \hat{\mathbf{n}} \times \hat{\mathbf{e}}_\beta. \tag{22}$$

Hence, the strain measures turn out to be:

$$\begin{aligned}\epsilon_\alpha &= \ln\left(|\mathbf{t}_\alpha|\right) & \epsilon_\beta &= \ln\left(\left|\mathbf{t}_\beta\right|\right)\\ \kappa_{\alpha\beta} &= \frac{\partial \hat{\mathbf{e}}_\alpha}{\partial \hat{\mathbf{v}}_1}\cdot\hat{\mathbf{m}}_\alpha & \kappa_{\alpha 3} &= \frac{\partial \hat{\mathbf{n}}}{\partial \hat{\mathbf{v}}_1}\cdot\hat{\mathbf{e}}_\alpha\\ \kappa_{\beta\alpha} &= \frac{\partial \hat{\mathbf{e}}_\beta}{\partial \hat{\mathbf{v}}_2}\cdot\hat{\mathbf{m}}_\beta & \kappa_{\beta 3} &= \frac{\partial \hat{\mathbf{n}}}{\partial \hat{\mathbf{v}}_2}\cdot\hat{\mathbf{e}}_\beta\end{aligned} \tag{23}$$

$$\begin{aligned}\tau_\alpha &= \frac{\partial \hat{\mathbf{m}}_\alpha}{\partial \hat{\mathbf{v}}_1}\cdot\hat{\mathbf{n}} & \tau_\beta &= \frac{\partial \hat{\mathbf{m}}_\beta}{\partial \hat{\mathbf{v}}_2}\cdot\hat{\mathbf{n}}\end{aligned} \tag{24}$$

therefore, the elastic energy W, assumed again as a quadratic form of the strain measures, can be defined as:

$$\begin{aligned}W = \frac{1}{2}\int_A & k_e\left(\epsilon_\alpha{}^2 + \epsilon_\beta{}^2\right) + k_{bp}\left(\kappa_{\alpha\beta}^2 + \kappa_{\beta\alpha}^2\right)\\ & + k_{bf}\left(\kappa_{\alpha 3}^2 + \kappa_{\beta 3}^2\right) + k_t\left(\tau_\alpha^2 + \tau_\beta^2\right) dA\end{aligned} \tag{25}$$

where k_e, k_t, k_{bp}, and k_{bf} have the same meaning of those in Eq. (13).

In order to determine such stiffness coefficients as a function of the gridshell characteristic properties, the same approach described in Section 2.3 is used.

An energetic equivalence between discrete and continuum models is enforced with respect to an equivalent area element whose sides are parallel to the directions defined by the angles α and β shown in Fig. 6. In particular, accounting for Eqs. (3) and (25), the energetic equivalence can be written as:

$$W = W_\alpha + W_\beta \tag{26}$$

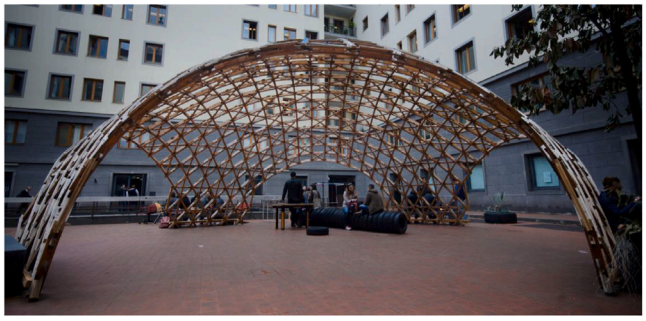

Fig. 7. Gridshell *Toledo 2.0* in the courtyard of the Faculty of Architecture in Naples, Italy 2014.

Table 1
Geometrical and mechanical properties of the *Toledo 2.0* discrete model.

E (MPa)	ν	A (m^2)	I_p (m^4)	I_f (m^4)	J (m^4)
12000	0.3	0.001	2.083E−7	3.33E−8	2.417E−7

where W_α and W_β are the elastic energy of the beams having length d and directed along the directions defined by the angles α and β.

Analogously to the procedure of Section 2.3, the energy equivalence must hold for any deformation mechanism. Therefore, assuming that the shell strain measures do coincide with those of the discrete system, the stiffness coefficients can be obtained by analysing separately the effect of each deformation mode, imposing that only the one associated with the unknown coefficient is non-zero. For example, if the elongation of the beams along the α-direction is the only non-zero strain component, as shown in Fig. 6, Eq. (26) yields:

$$\frac{1}{2}\int_L EA{\epsilon_\alpha}^2\, dL = \frac{1}{2}\int_A k_e{\epsilon_\alpha}^2\, dA \tag{27}$$

so that

$$k_e = \frac{EA}{d} \tag{28}$$

hence, the remaining stiffness coefficients turn out to be

$$k_{bp} = \frac{EI_p}{d} \quad k_{bf} = \frac{EI_f}{d} \quad k_t = \frac{GJ}{d} \tag{29}$$

where I_p, I_f and J have the same meaning of the previous section.

In conclusion, the model formulation presented in this section and based on the energetic equivalence yields a non-conventional Kirchhoff–Love shell. Actually, it incorporates both membrane and plate (bending) behaviour and presents additional energetic contributions associated with the in-plane bending of the bars $\kappa_{\alpha\beta}$ and $\kappa_{\beta\alpha}$, which are not typical of the traditional shell formulation. Moreover, in the case of two orthogonal rod registers, the resulting constitutive law specializes to an orthotropic shell.

3. Numerical simulations

In order to validate the continuum equivalent model presented in Section 2, numerical simulations are hereby presented. In particular, the first investigated model consists of an octagonal gridshell with orthogonal rods whose dimensions and mechanical properties have been calibrated so that the model reproduces *Toledo 2.0*, the post formed timber gridshell prototype [32].

Such a model was erected in 2014 and it is shown in Fig. 7. Its construction process is described in Section 4.

A further model consists of a rectangular gridshell made up of non-orthogonal rods, in order to validate the extension of the presented model, described Section 2.4.

Each model has been modelled in *COMSOL Multiphysics*® [30] adopting Hermite cubic (*quad* and *tria*) shell elements, in order to ensure C^1 continuity of the displacement field, and implementing a Total Lagrangian Formulation, thus accounting for large strains and displacements. The constitutive behaviour has been modelled so that their elastic energy is defined by Eq. (13).

The nonlinear solution is obtained with the Automatic Highly Nonlinear (Newton) algorithm of *COMSOL Multiphysics*®, an affine-invariant damped Newton method with dynamic step-length control. In all the performed analyses the solver starts from a strongly reduced initial damping factor of 10^{-4} and enforces a minimum damping as low as 10^{-8}, cautiously increasing the step only when the residual reduction is satisfactory. Such an algorithm is designed to improve global robustness on strongly nonlinear problems at the price of additional Newton iterations. Besides the method can over-increase the computational burden, we deliberately decided to use the most robust solver available in the framework, as the convergence behaviour of the model under investigation was *a priori* unknown.

As it commonly occurs in the numerical simulation of thin shells, the finite element implementation of the equivalent model is potentially affected by locking phenomena. To mitigate such effects, standard strategies have been adopted within the *COMSOL Multiphysics*® framework.

The results of the analysis relevant to such a continuum model have been compared with the outcomes of discrete rod models analysed in *MARC*® *Mentat*® [31]. These consist of rods grid made of large displacement beam element (i.e. *Element 52*). Coherently with Eq. (13), all rods are assumed to lie in the same plane. At joints, an internal connection between nodes belonging to the two different registers constraints translations and in-plane rotations in order to permit drilling. The *Toledo 2.0* model presents a squared shape with a width of 10.5 m and its four corners are removed, as shown in Fig. 8(a). The corners are sliced in order to connect foundations. The finite element models adopting the continuum formulation and the beam discretization are reported in Figs. 8(b) and 8(c), respectively. Square elements with side of 0.25 m are used in the continuum model (4 triangular elements are used on each corner), while line elements of 0.1 m are used to model the beams of the discrete model. This results in 1740 elements with 1809 nodes for the continuum model and in 4500 elements with 4546 nodes for the discrete model. The rods present a 5 × 2 cm rectangular cross section, while their geometrical and mechanical properties are reported in Table 1. We remark that the value of the Young's modulus E was set in accordance with the technical data sheets supplied by local manufacturers for larch profiles; although the elastic modulus of wood may exhibit significant variability, the analyses reported here and in Section 4 are essentially insensitive to its precise value. In fact, the models analysed in this section are driven by prescribed displacements, so that the total potential energy coincides with the elastic strain energy and E enters as a constant that does not affect the stationarity conditions. Concerning the experimental comparison in Section 4, it is performed solely in terms of the deformed configuration, which depends only weakly on E (whereas internal forces and support reactions, on which the Young's modulus has a stronger influence, are not available for the experimental case).

3.1. In-plane tensile loading

A first numerical application consists of an in-plane tensile test of the *Toledo 2.0* model, see, e.g., Fig. 8. In particular, boundary conditions are defined so that the relative displacements of the nodes of the edges AB and EF are unconstrained, while the translation along z-axis is constrained. Loading is assigned by enforcing a fixed displacement of 1 m along the direction oriented at 45° with respect to the x-axis, to the edges AB and EF in Fig. 8. Such a load case is crucial for testing that the model effectively reproduces the zero-energy shear mechanism typical of gridshells and essential for enforcing double-curvature in case of out-of-plane deformative processes.

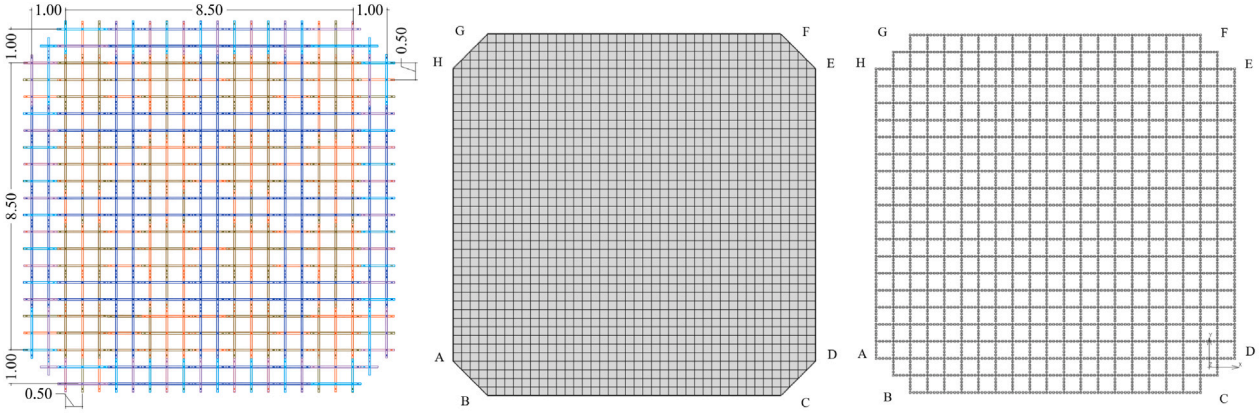

(a) Undeformed configuration; (b) FEM continuum model (mesh size = 0.25 m); (c) FEM discrete model (mesh size = 0.1 m);

Fig. 8. Schemes of the *Toledo 2.0* model (undeformed configurations).

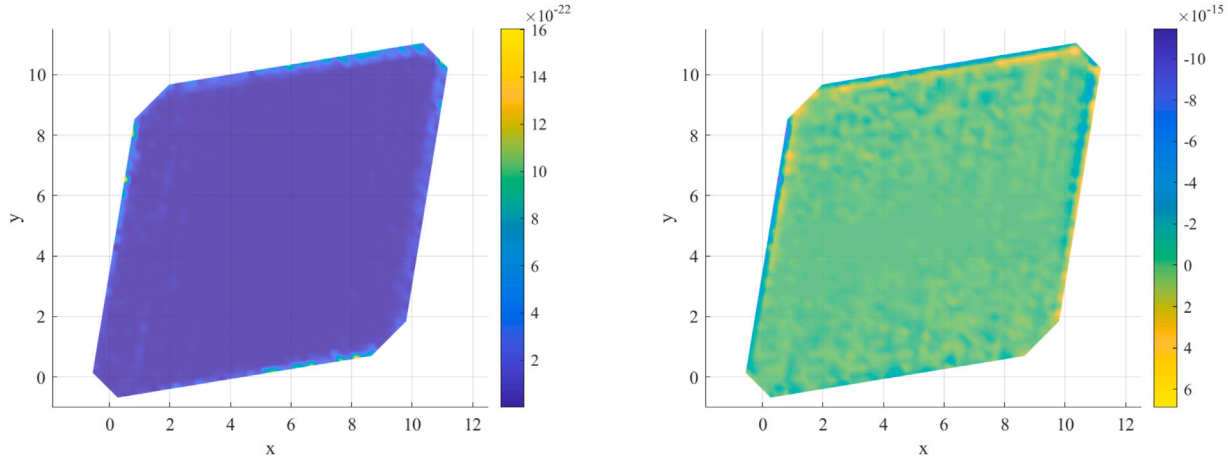

(a) Elastic energy W; (b) Strain component ϵ_x;

Fig. 9. In-plane pure-shear rigid mechanism of the continuum model for the *Toledo 2.0* gridshell.

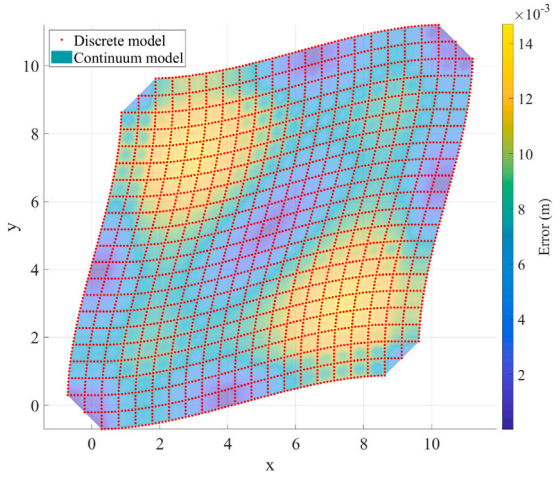

Fig. 10. Superposition of the equilibrium configurations of the continuum and discrete model for the *Toledo 2.0* gridshell subjected to an in-plane tensile loading.

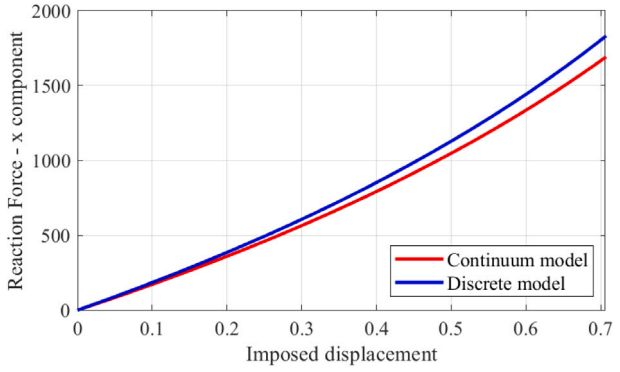

Fig. 11. Constraint reaction vs. displacement of the continuum and discrete models for the *Toledo 2.0* gridshell subjected to an in-plane tensile loading.

Fig. 9 reports the deformed configuration of the model as well as the colourmaps of the elastic energy W (Fig. 9(a)) and of the strain component ϵ_x (Fig. 9(b)). Actually, such a configuration is associated with pure-shear deformation at all points of the domain; in fact, both energy and the normal strain component turn out to be null.

Although such a behaviour was expected on the basis of the theoretical formulation, in particular the fact that in-plane shear strain component is not relevant to any energetic contribution in Eq. (13),

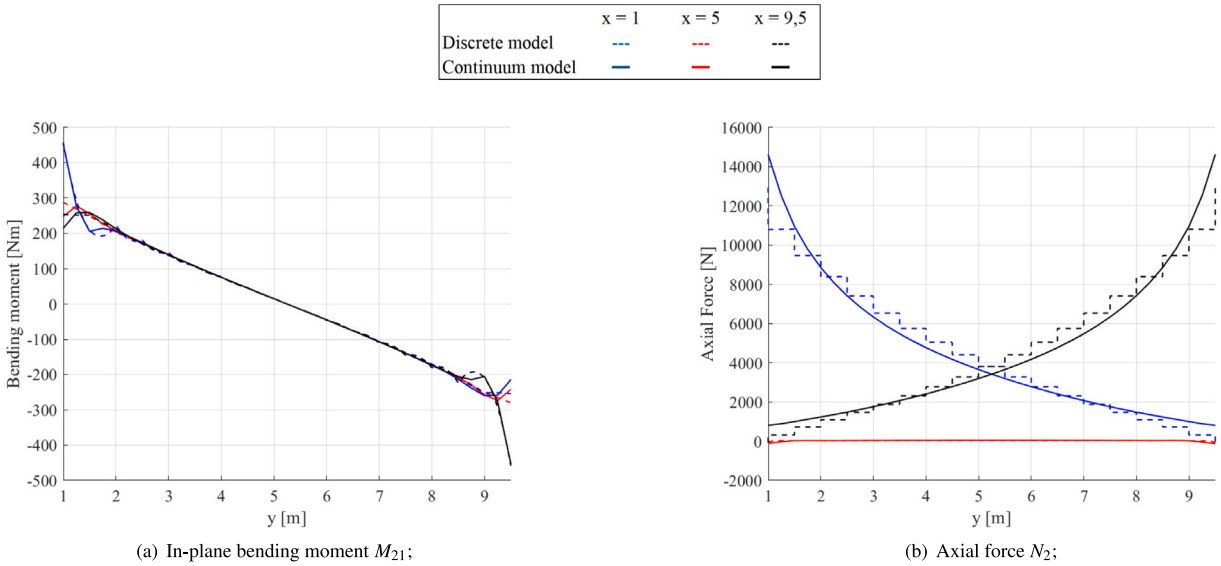

(a) In-plane bending moment M_{21}; (b) Axial force N_2;

Fig. 12. Internal forces of the continuum (solid curves) and discrete model (dashed curves) relevant to y-aligned beams at $x = 1$ m (blue curves), $x = 5$ m (red curves) and $x = 9.5$ m (black curves) for the *Toledo 2.0* gridshell subjected to an in-plane tensile loading. (For interpretation of the references to colour in this figure legend, the reader is referred to the web version of this article.)

Table 2
Errors.

N. Application	L_x (m)	L_y (m)	H_{max} (m)	$\bar{\mathcal{E}}$ (cm)	$\hat{\mathcal{E}}$
Tensile loading	10.5	10.5	–	0.8	1.0%
Buckle loading	10.5	10.5	3.2	0.9	1.7%
Barrel Vault 1	58.14	29.07	7.6	7.7	1.7%
Barrel Vault 2	58.14	29.07	4.5	3.7	1.3%

this numerical test confirms that no parasite phenomena arise in the continuum numerical analysis.

In-plane actions can be triggered by enforcing different constraint conditions. Specifically, if the stretching of sides AB and EF is blocked (i.e. the relative displacements of the nodes of the edges AB and EF are constrained) and a fixed displacement of 1 m along the direction oriented at 45° with respect to the x-axis is enforced, the model is subject to pure-membrane actions, as shown in Fig. 10 reporting the deformed configuration at the end of the deformative process.

The red lines represent the discrete model analysed with *MARC*® *Mentat*®, while the continuum one is represented by the surface. The colourmap shows the numerical pointwise error between the models computed as the norm of the vector collecting the displacement difference between corresponding points in the undeformed configuration of the discrete and continuum models. The dimensional error, computed as the Mean of the Norm of the Vector Displacement Difference, denoted by $\bar{\mathcal{E}}$, is approximately 8 millimetres, while the corresponding percentage error, denoted by $\hat{\mathcal{E}}$, is 1.0%, as reported in Table 2.

Concerning static responses, Fig. 11 report the reaction-displacement curves of the continuum and discrete models. The reaction is the norm of the resultant of the constrained nodes belonging to one of the constrained corners (i.e. side AB in Fig. 8(b)) and is plotted as function of the displacement enforced at the same corner. Due to symmetry, both the displacement and the reaction turn out to be oriented towards the diagonal of the model. In particular, the continuum model underestimates the constraint reaction.

Such differences are likely related to boundary effects due to the perimeter rods. Since energetic equivalence is imposed at the level of the elementary area, each rod contributes the same energy as a continuum strip of width equal to the rod spacing. As a result, the boundary of the continuum model, having the same perimeter as the discrete one, approximatively accounts for only half of the energy of the corresponding discrete rods. For instance, in the uniaxial tensile case with n rods spaced by d, the discrete width is $d(n-1)$, while the energetically equivalent continuum width is nd. In more general cases, estimating the necessary continuum expansion is less straightforward, and is deferred to future work.

Internal forces of the continuum and discrete model are reported in Fig. 12. These are relevant to y-aligned beams located at $x = 1$ m (blue curves), $x = 5$ m (red curves) and $x = 9.5$ m (black curves). Because of the load conditions, the out-of-plane bending moment and the torque turn out to be null; hence the graphs report the in-plane bending moment M_{21} (Fig. 12(a)) and the axial force N_2 (Fig. 12(b)). Internal forces of the continuum model have been computed by multiplying the local generalized stress value by the width of the equivalent area.

Both the constraint reaction and the internal forces exhibit a good agreement. Hence, the comparative assessment of in-plane deformations between the continuum and discrete models reveals remarkable agreement. Both qualitative comparisons and quantitative error analyses, characterized by exceptionally low dimensional and percentage error values, substantiate the very good agreement between the two modelling approaches. These findings not only validate the continuum model's predictive capabilities but also confirm its reliability as a computational framework for analysing in-plane deformational behaviours.

3.2. Controlled buckling

A further numerical application, aiming to investigate the out-of-plane behaviour, involves a different load case applied to the *Toledo 2.0* model. Specifically, a fixed displacement of 1 m is now applied to the four edges AB, CD, EF, GH. It is applied horizontally along the direction orthogonal to each edge and oriented towards the centre of the model, in order to buckle the structure and obtain a curved gridshell. Again, the relative displacement of the nodes belonging to each edge is blocked, as in the previous case.

Such an application permits to investigate how the continuum model behaves when we introduce flexural strain measures to account for out-of-plane motions.

The results are presented in Fig. 13 where equilibrium configurations at the end of the deformative process are shown. Specifically, the red lines show the configuration of the discrete model, while the surface

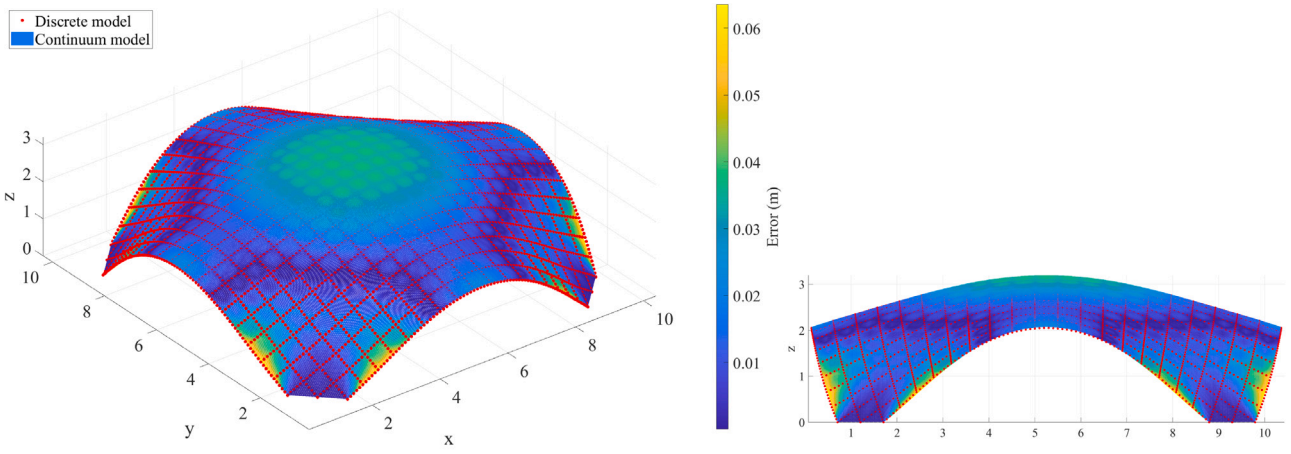

(a) Axonometric view; (b) Front view;

Fig. 13. Superposition of the equilibrium configurations of the continuum and discrete model for the *Toledo 2.0* gridshell subjected to an out-of-plane buckle loading. (For interpretation of the references to colour in this figure legend, the reader is referred to the web version of this article.)

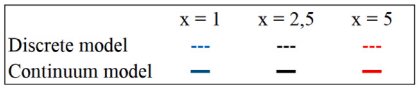

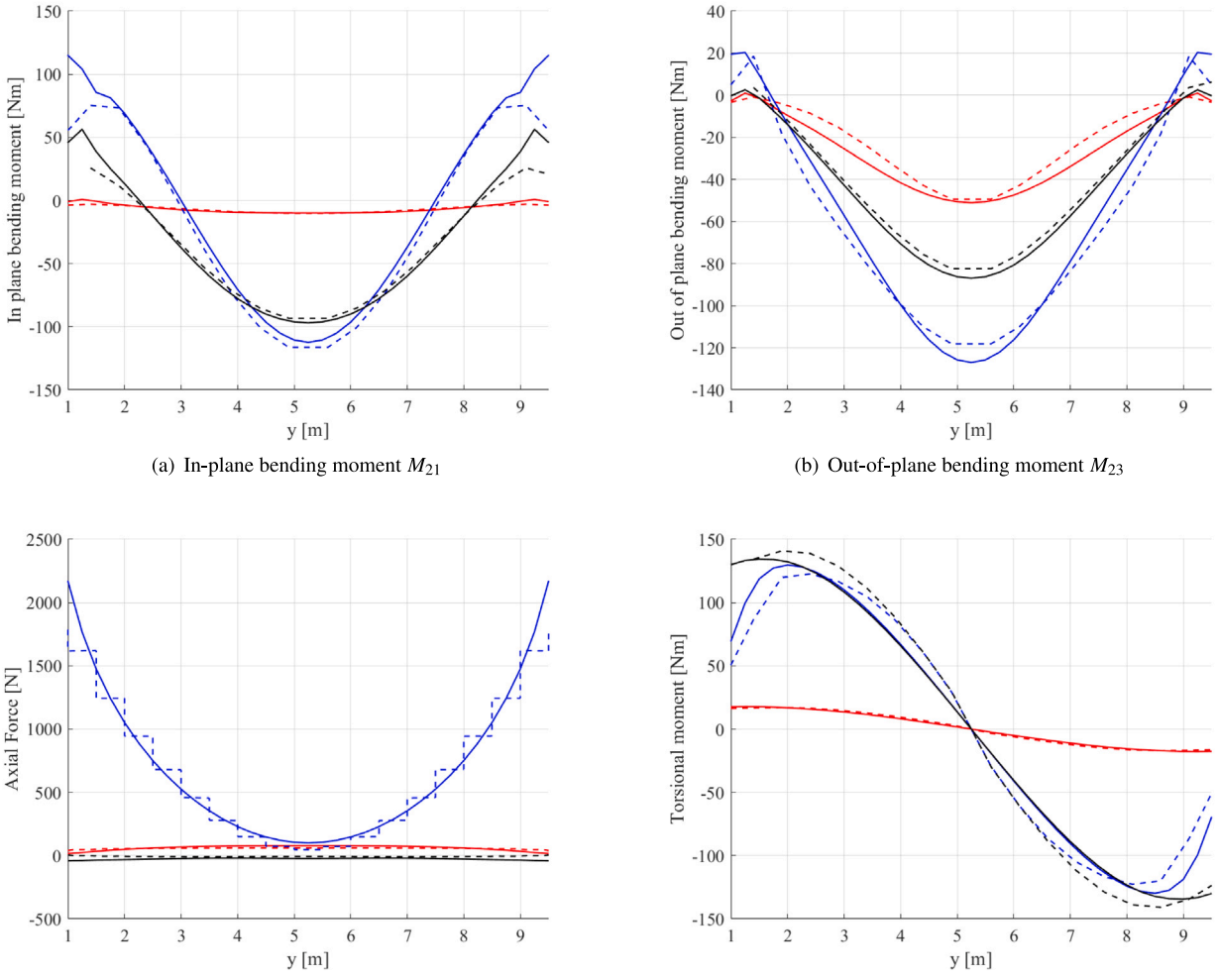

(a) In-plane bending moment M_{21} (b) Out-of-plane bending moment M_{23}

(c) Axial force N_2 (d) Torsional moment T_2

Fig. 14. Internal forces of the *Toledo 2.0* gridshell subjected to an out-of-plane buckle loading computed for the Continuum (solid curves) and Discrete (dashed curves) models relevant to y-oriented rods at $x = 1$ m (blue curves), $x = 2.5$ m (black curves), and $x = 5$ m (red curves). (For interpretation of the references to colour in this figure legend, the reader is referred to the web version of this article.)

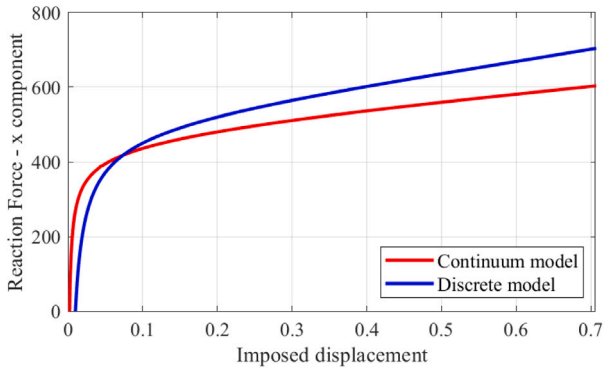

Fig. 15. Constraint reaction vs. displacement of the *Toledo 2.0* gridshell subjected to an out-of-plane buckle loading.

Table 3
Geometrical and mechanical properties of the Grid Vault model with non-orthogonal bundles.

E (MPa)	ν	A (m^2)	I_p (m^4)	I_f (m^4)	J (m^4)
12000	0.3	0.0025	5.208E−7	5.208E−7	1.04E−6

represents the continuum one. The colourmap represents the numerical pointwise error between the two models, computed as in the previous load case. The dimensional error $\bar{\mathcal{E}}$ has a value of 9 millimetres, while the percentage error $\hat{\mathcal{E}}$ is 1.7%.

As for the in-plane loading case, a further comparison between the continuum and the discrete model has been performed in terms of static responses. In particular, Figs. 14 report the diagrams of the internal forces computed by the continuum (solid curves) and discrete model (dashed curves) relevant to three y-aligned beams located at $x = 1$ m, $x = 2.5$ m, and $x = 5$ m. Since the deformative process involves both membrane and flexural contributions, the models present four components of the internal forces, i.e. in-plane and out-of-plane bending moments, reported in Figs. 14(a) and 14(b), respectively, the axial force, reported in Fig. 14(c) and the torsional moment, shown in Fig. 14(d).

Generally, internal forces exhibit a good agreement between the continuum and the discrete model, although some discrepancies are visible at the edges of the diagrams. These are induced by local effects due to the boundaries nearby the constrained regions, as confirmed by the constraint reaction diagrams reported in Fig. 15. In particular, analogously to the previous numerical test, the graph shows the value of the constraint reaction resultants relevant to one of the model's corners as function of the corresponding horizontal displacement. The red curve reports the reaction of the continuum model while the blue curve is relevant to the discrete one. As a matter of fact, the curves exhibit a fair agreement although an error, consistent with the internal forces of Fig. 14, is visible. Such an issue has already been discussed in the previous section and does not compromise the computation.

In conclusion, the controlled buckling test of the *Toledo 2.0* gridshell confirms the capability of the continuum formulation to accurately capture both membrane and flexural behaviours, providing results in good agreement with the discrete model even in complex out-of-plane deformation scenarios.

3.3. Gridshell with non-orthogonal rods

In order to investigate the case of non orthogonal grid, a final numerical example is presented. The model consists of a rectangular shape with dimensions of $L_x = 58.14$ m and $L_y = 29.07$ m. The two sets of beams are aligned along the diagonals of the rectangle, so that

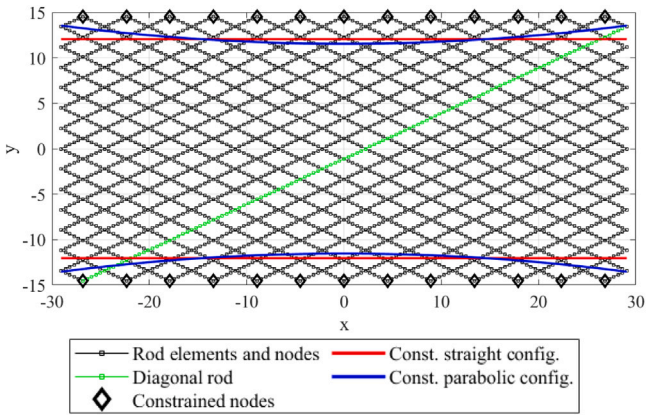

Fig. 16. Non–orthogonal gridshell model. Discrete model rods and nodes (black), constrained nodes (green), target constraint configurations: straight (red) and parabolic (blue). (For interpretation of the references to colour in this figure legend, the reader is referred to the web version of this article.)

their orientations are:

$$\hat{\boldsymbol{v}}_1 = \cos(\alpha)\mathbf{E}_1 + \sin(\alpha)\mathbf{E}_2$$

$$\hat{\boldsymbol{v}}_2 = \cos(\beta)\mathbf{E}_1 + \sin(\beta)\mathbf{E}_2$$

where

$$\alpha = \tan^{-1}\left(\frac{L_y}{Lx}\right) \quad \beta = \pi - \alpha.$$

Rod spacing is 2 m so that we have 26 parallel beams for each bundle with geometrical and mechanical properties reported in Table 3.

The discretized model is reported in Fig. 16 where the black lines and squares represent the rods and the nodes. Line elements of 0.25 m are used to model the rods.

The continuum model, instead, consists of a rectangle, with dimension L_x and L_y. Square elements with side of 1 m are used for the two-dimensional mesh.

Again, two load cases have been adopted. In the first case, a fixed displacement of 2.5 m is imposed along the y-direction, uniformly for all nodes along the x-direction, at both the outer long edges of the rectangle in order to buckle the structure and create a sort of barrel vault. In the second case, a horizontal displacement is enforced so that the constrained long edges assume a parabolic in-plane configuration. Specifically, the x-displacement of the nodes along the outer long edges are nil, while the y-displacement is given through a parabolic pattern and assumes, at each node, a value related to the node position by the following expression

$$d_y = -\frac{8}{L_x^2}x^2 + \frac{8}{L_x}x + 1 \tag{30}$$

where d_y is the y-displacement and x is the x-coordinate of the node. This results in a 1 m displacement at the corners and in a 3 m displacement at the midpoints.

The second load case was specifically designed to achieve a more pronounced double-curvature deformation, a typical configuration commonly sought in gridshell constructions. By applying differential displacement along the long edges, we induce a more complex spatial morphology that better represents the geometric potential and structural behaviour of gridshell systems.

The constraint nodes of the discretized model are represented as black diamonds in Fig. 16, where the constraint alignment of the first and second deformative processes are represented in red and blue, respectively. Moreover, the green beam represents the diagonal rod for which internal forces are reported below. Constraint motion of the continuum model has been enforced by means of differential boundary conditions.

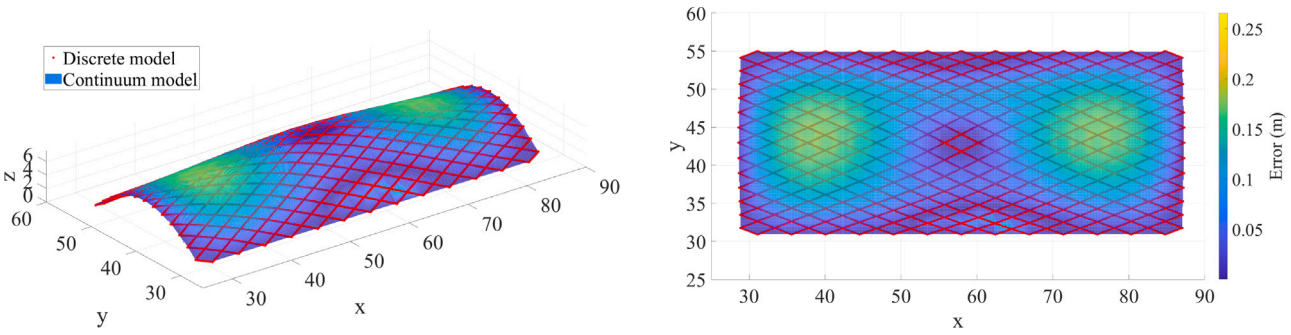

(a) Axonometric view; (b) Top view;

Fig. 17. Comparison between the equilibrium configurations of the continuum (surface) and discrete model (red lines): error colourmap. Barrel Vault Type I. (For interpretation of the references to colour in this figure legend, the reader is referred to the web version of this article.)

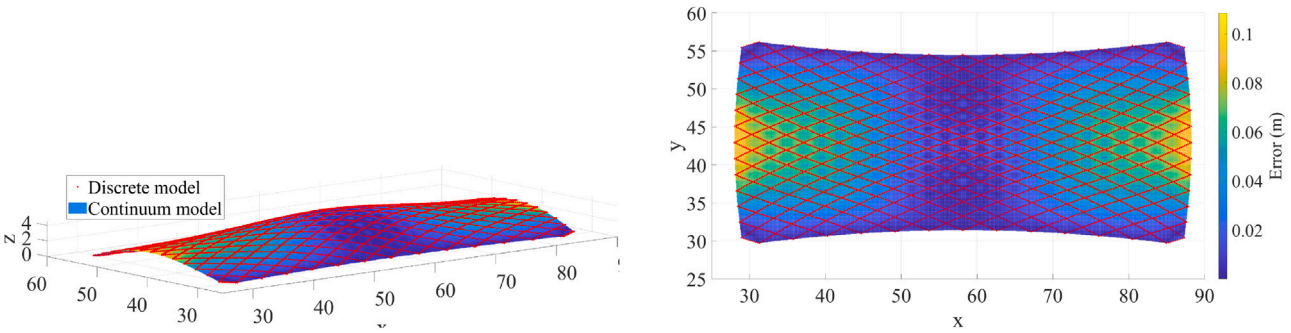

(a) Axonometric view; (b) Top view;

Fig. 18. Comparison between the equilibrium configurations of the continuum (surface) and discrete model (red lines): error colourmap. Barrel Vault Type II. (For interpretation of the references to colour in this figure legend, the reader is referred to the web version of this article.)

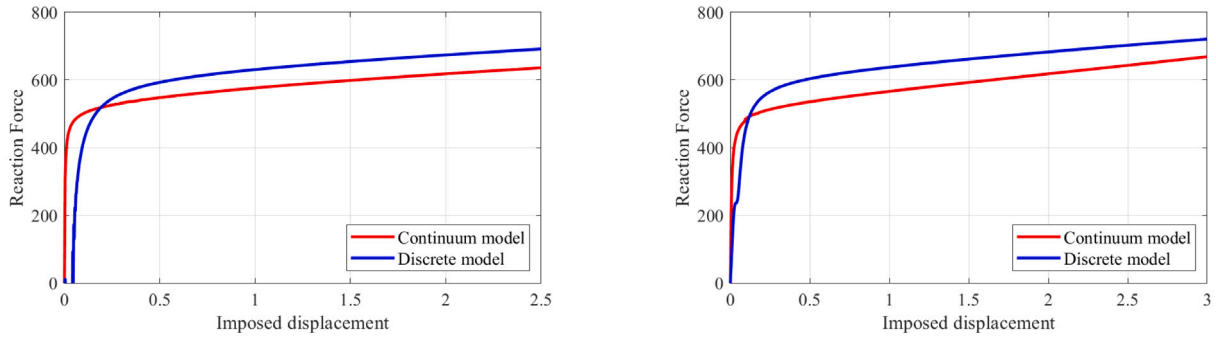

(a) Type I; (b) Type II;

Fig. 19. Constraint reaction vs. displacement of the Barrel Vault.

For the first load case, the dimensional error $\bar{\mathcal{E}}$ is 7.7 cm, with a corresponding percentage error $\hat{\mathcal{E}}$ of 1.7%. For the second load case, these values are 3.7 cm and 1.3%, respectively. Again, the numerical outcomes show a good accuracy of the continuum model in reproducing the deformative behaviour of the discrete one. Table 2 summarizes the error values for each numerical application.

The results associated with both load cases are reported in Figs. 17 and 18, relevant to the straight and the parabolic pattern of constraint displacements, respectively. Such Figures show the deformed configurations of the discrete and continuum models at the end of the deformative process. In particular, the discrete model is represented by the red lines, while the continuum one is represented as a surface. As in the previous example, the colourmap represents the pointwise error.

Fig. 19 reports the diagrams of the component of the resultant of the constraint reactions, relevant to a single side of the gridshell, computed as function of the imposed displacement for both the deformative processes.

Moreover, Figs. 20 and 21 report the diagrams of the internal forces relevant to Type I and Type II deformation processes, respectively. Such forces are relevant to the diagonal beam drawn in green in Fig. 16.

As a matter of fact, the continuum internal forces exhibit a remarkable agreement with the discrete model although the homogenized analysis is not capable of reproducing the discontinuities relevant to the rod joints.

On the contrary, constraint reactions present an error, analogously to the previous examples. As for the cases discussed above, this is

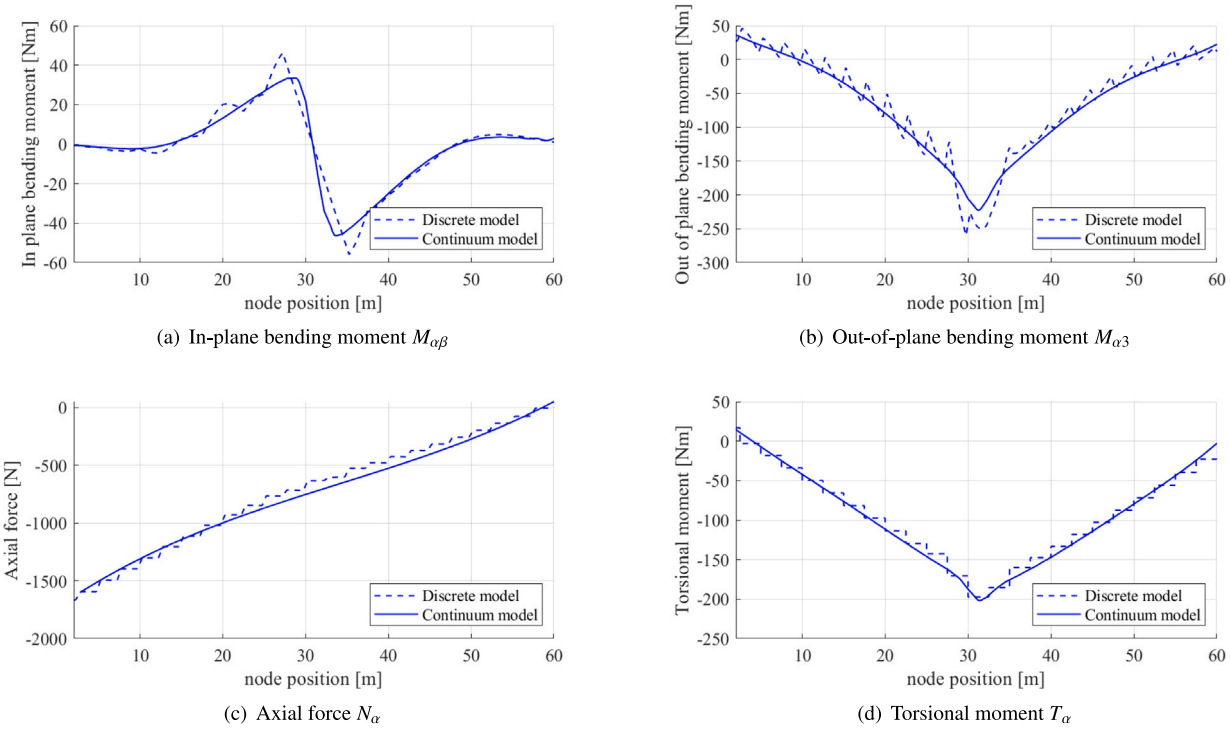

(a) In-plane bending moment $M_{\alpha\beta}$ (b) Out-of-plane bending moment $M_{\alpha 3}$

(c) Axial force N_α (d) Torsional moment T_α

Fig. 20. Internal forces of the *Barrel Vault Type I* gridshell subjected to an out-of-plane buckle loading computed for the Continuum (solid curves) and Discrete (dashed curves) models relevant to the diagonal rod.

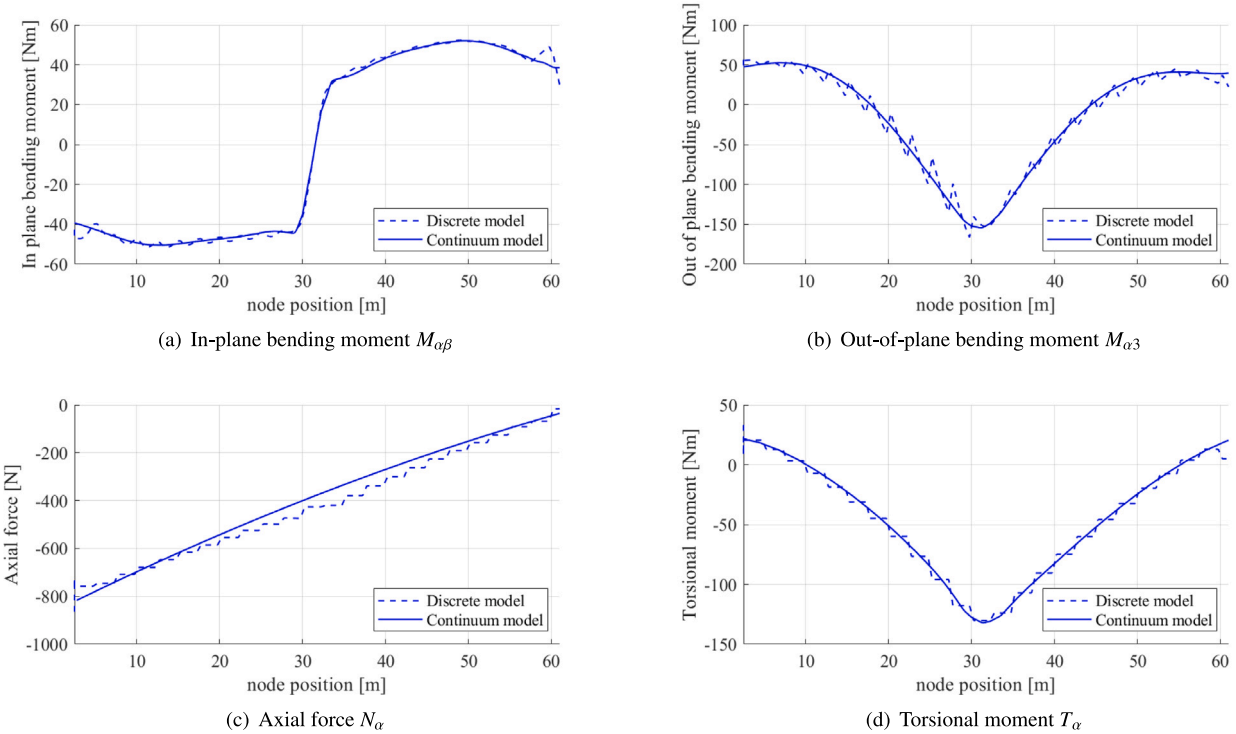

(a) In-plane bending moment $M_{\alpha\beta}$ (b) Out-of-plane bending moment $M_{\alpha 3}$

(c) Axial force N_α (d) Torsional moment T_α

Fig. 21. Internal forces of the *Barrel Vault Type II* gridshell subjected to an out-of-plane buckle loading computed for the Continuum (solid curves) and Discrete (dashed curves) models relevant to the diagonal rod.

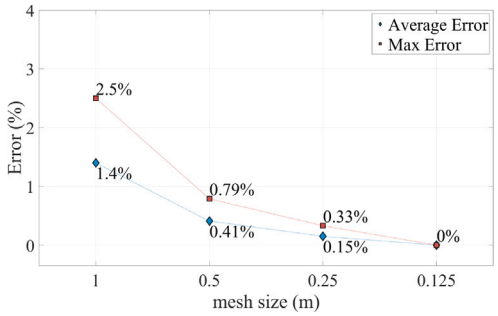

(a) *Toledo 2.0* tensile loading

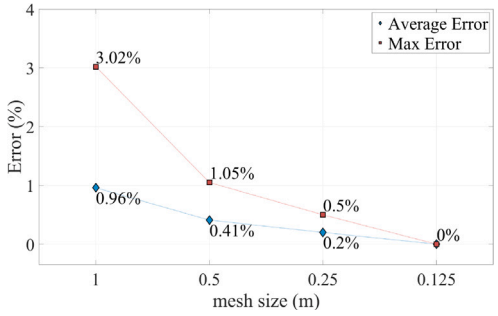

(b) *Toledo 2.0* buckle loading

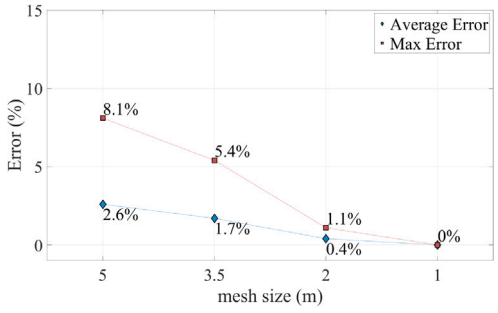

(c) Barrel Vault Type I

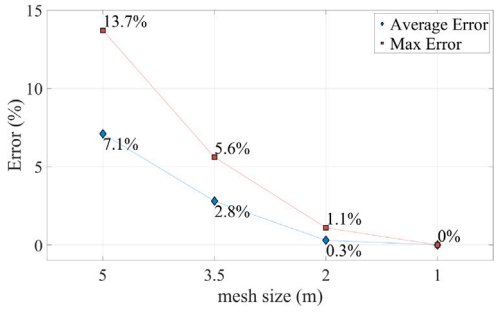

(d) Barrel Vault Type II

Fig. 22. Mesh sensitivity: Plot of the relative error of each mesh with respect to the finest mesh.

related to boundary effects and does not compromise the general computation.

3.4. Mesh sensitivity

To assess the accuracy of the proposed numerical model, a convergence study has been performed in order to evaluate the sensitivity of the solution with respect to the mesh size.

Table 4
Mesh size for the convergence analysis.

Element size:	#1	#2	#3	#4
Toledo 2.0	1 m	0.5 m	0.25 m	0.125 m
Barrel Vault	5 m	3.5 m	2 m	1 m

Sensitivity of the response with respect to the mesh discretization has been investigated by adopting four different mesh spacings for both the Toledo 2.0 model and the Barrel Vault. Element sizes relevant to each mesh spacing are reported in Table 4.

Loads protocols is analogous to those adopted in Section 3, as well as the strategy for computing the error. In particular Fig. 22 shows the average and the maximum percentage error as a function of the mesh size for all the considered models. In such a case, errors have been computed with reference to the models having mesh size #4. Results show that the computed response is reasonably stable as the elements size grows.

3.5. Estimation of torque induced by rods' eccentricity

Coplanarity of the rod registers assumed by both the investigated continuum model and the discrete one ignores the eccentricity usually introduced by connections. Hence, coupling between axial forces and torsional moments is neglected so as additional parasite torque contributions is induced, as discussed in Section 2.2.

Indeed, Toledo 2.0 gridshell was built by connections made of steel bolts orthogonal to the rods, thus resulting in an eccentricity of 2 cm.

In order to validate the investigated model, an estimate of such a parasite torque has been computed and is hereby presented. In particular, it has been computed by determining the axial force unbalance between two subsequent rods at each joint. This has been multiplied by the rod eccentricity in order to get the parasite torque.

Figs. 23(a) and 23(b) report the absolute value of the ratio between the parasite torque and the computed torsional model for the Toledo 2.0 model and the barrel vaults, respectively, relevant to the beams whose torsional moments are shown in Figs. 14(d), 20(d) and 21(d).

Indeed, the maximum value of the computed ratios is about 10% while it turns out to be far smaller for most of the rod sections. This is related to two aspects. On the one hand, dimensions of the rods of the Toledo 2.0 model were small enough to induce limited eccentricity. On the other hand, during the development phase (when no bracing system is present) the axial force exhibits very limited unbalances across the hinges.

Such a result proves that the approximation introduced by rod coplanarity does not significantly affect the numerical results. Nevertheless, the model should be used carefully in the case of joint technologies presenting high eccentricities as well as in presence of membrane stiffening systems.

The error estimation presented in this section can be a useful tool for checking *a posteriori* if the continuum model is suitable for the analysed model.

4. Comparison with experimental evidence

A comparison between experimental results and numerical predictions is presented in this section in order to confirm the effectiveness and the accuracy of the proposed model. We will refer to D'Amico et al. [32], in which the construction process of the Toledo 2.0, a post-formed timber gridshell erected in 2014, is described. The initial process involved laying the flat mat on the ground and subsequently elevating it to its ultimate configuration. As depicted in Figs. 24(a)–24(c), eight central gridshell nodes were lifted using a pulley system positioned atop a central scaffolding tower, using four nautical-grade cables and four manual hoists. Upon achieving the gridshell's desired height, two supplementary cross cables and hoists were incorporated at the

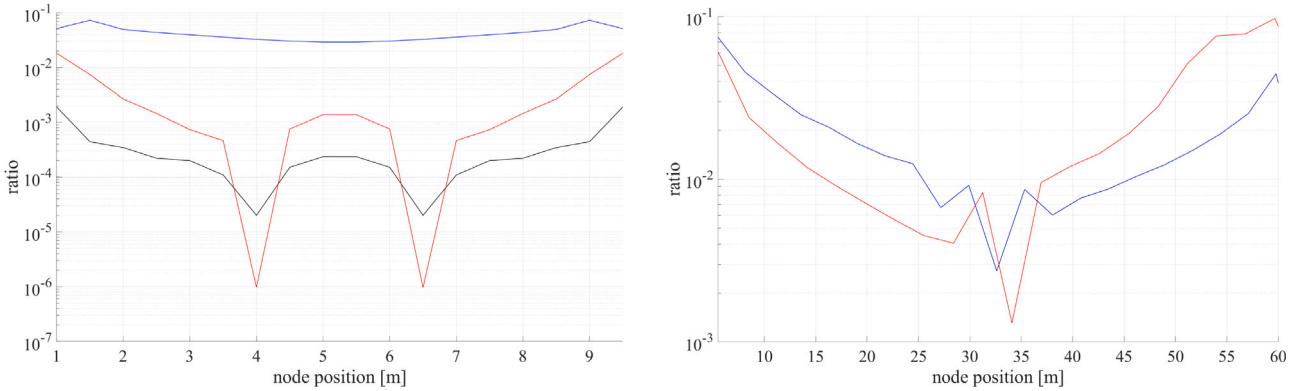

(a) *Toledo 2.0* with out-of-plane buckle loading. Curves relevant to y-oriented rods at x = 1m (blue curves), x = 2.5m (black curves), and x = 5m (red curves).

(b) Barrel Vault Type I (blue curve) and Type II (red curve).

Fig. 23. Ratio between parasite torque induced by rod eccentricity and the torsional moment computed by the investigated models. Vertical axes in logarithmic scale. (For interpretation of the references to colour in this figure legend, the reader is referred to the web version of this article.)

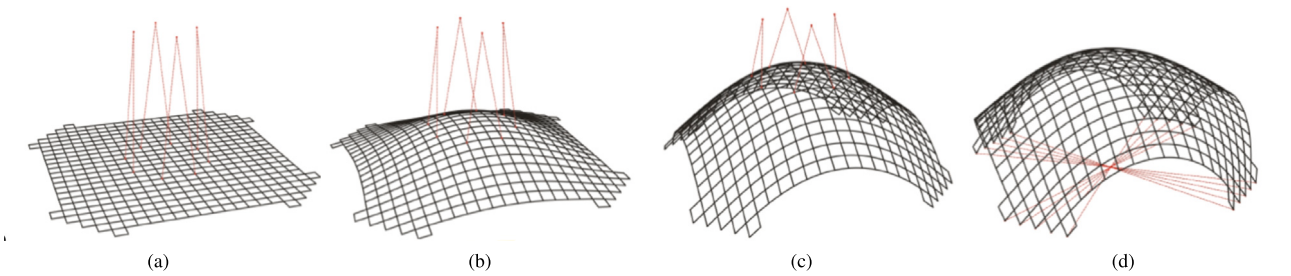

Fig. 24. Simulation of the deformation process: (a–c) The corner nodes are restrained on rollers while the central nodes are lifted up by cables; (d) Corner nodes are constrained by additional cables and the vertical lifting is disabled.

peripheral nodes to provide horizontal stabilization, thereby enabling the attainment of the desired geometric configuration, as illustrated in Fig. 24(d). Finally, two additional bundles of diagonal rods, aiming to freeze the membrane configuration, were mounted. Such diagonals have been not included in the computations since they were not present during the deformative process although they are clearly visible in Figs. 7 and 25(a), both showing the final configuration of the gridshell.

4.1. Geometric survey

The *Toledo 2.0* gridshell was object of a survey procedure focused on the localization of node position, and based on photogrammetry and 3D scanning. Fiducial markers were placed on the extrados, as shown in Fig. 25(a), so that a mobile camera was able to capture overlapping images. These were processed by a Structure-from-Motion algorithm so that the sparse position of the markers was determined.

Subsequently, a Scale-Invariant transformation was used to refine the 3D reconstruction. The procedure, whose details are reported in the paper by Colabella et al. [38], was validated by a further 3D laser scan survey that confirmed the accuracy of the detected model. The latter is shown in Fig. 25(b) and its markers' locations will be used as benchmark for the investigated continuum model.

4.2. Results

The geometrical characterization of the deformed configuration detected by the survey permitted to determine the path of the deformation process, schematized in Fig. 24, that can be adopted within the finite element analysis. In particular, such a computational loading path aims to reproduce the real building process. To this end, a first loading process consisted of 8 vertical forces located at the points corresponding to the lifting cables' connections. These actions have been linearly increased until their application points reached a vertical displacement of 3.6 m (Fig. 24(b)), corresponding to the survey outcome. During such a loading process, the nodes of the four edges AB, CD, EF, and GH have been vertically constrained. For this reason, they can freely move on the horizontal plan and tend to displace towards the centre of the model.

Once the vertical lifting phase has been completed, enforcement of the horizontal cables has been modelled by introducing horizontal constraints to the nodes of the four edges AB, CD, EF, and GH. Therefore, their location has been modified by a displacement-control loading process in order to make them achieve their final location detected by the survey (Fig. 24(d)). Finally, the vertical forces have been linearly decreased to zero.

Since the survey detected only the geometry of the final configuration of the structure, it is not possible to establish a direct relationship between the real and the computational models in their undeformed configurations, being that of the real structure unknown. For this reason, the error estimate has been computed as the difference between the vertical locations of the marker points in the deformed configuration.

Fig. 26 shows the final deformed configuration of the continuum model, represented as a surface, compared to the experimental points, represented in red. The colourmap denotes the pointwise error computed as follows. Since the experimental data consist solely of a point cloud representing the deformed configuration, a direct comparison of displacement vectors is not feasible. To address this, we employ a

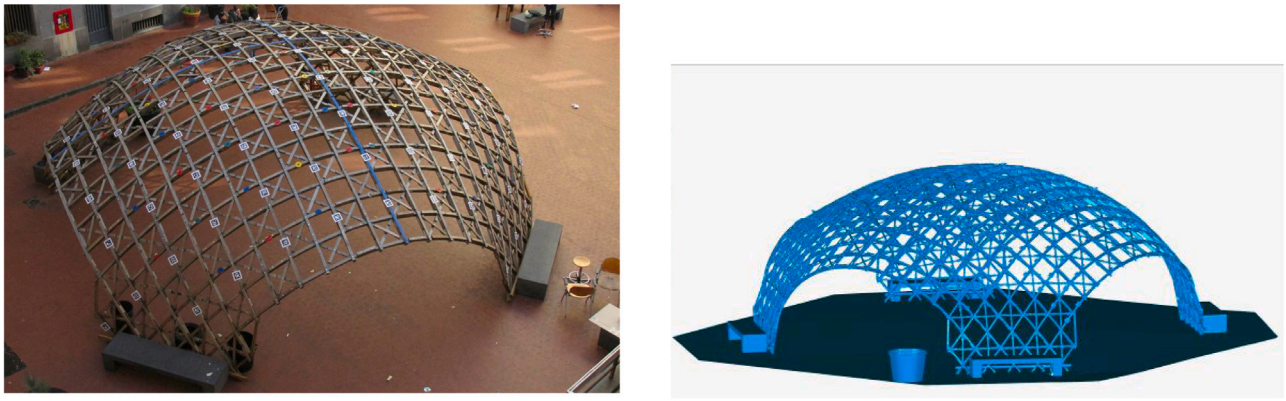

(a) Gridshell final configuration and markers; (b) Detected deformed configuration;

Fig. 25. Toledo 2.0 gridshell geometrical survey.

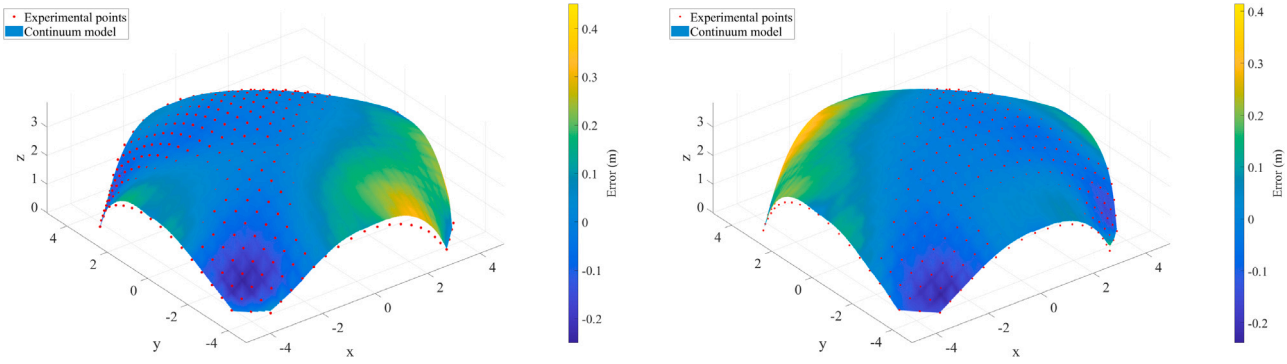

(a) Front view; (b) Back view;

Fig. 26. Comparison between experimental data and the results of the continuum model. (For interpretation of the references to colour in this figure legend, the reader is referred to the web version of this article.)

surface fitting technique to approximate the experimental data. The point error is then quantified by computing the pointwise difference in the z-coordinates between the fitted surface and the numerical model's corresponding deformed surface. The Error Root Mean Square $\tilde{\mathcal{E}}$ has a value of 9 centimetres, while Percentage Error Root Mean Square $\tilde{\mathcal{E}}_{\%}$ is 8%.

5. Conclusions

We developed a novel equivalent continuum shell model for gridshell structures deforming in a three-dimensional space, leveraging the Special Cosserat theory of rods. The model is intended for elastic gridshell deployment, i.e. before the installation of bracing systems. In this stage, drill and shear modes play a crucial role and cannot be captured by a classical Cauchy continuum, whereas for braced gridshells the distinction between the two formulations would be far less significant. The proposed approach offers significant advantages in numerical modelling and computational efficiency compared to traditional discrete beam element methods.

Four numerical simulations were conducted to validate the proposed model, comparing it with a discrete beam element representation. The results demonstrated remarkable accuracy, with a maximum percentage root mean square error of about 2% across different application cases. This high degree of precision validates the effectiveness of the continuum shell modelling approach for gridshell structures.

The comparative analysis revealed not only computational accuracy but also notable methodological advantages. While computational times were comparable between the two modelling approaches, the continuum model demonstrated a substantially more streamlined modelling process. The finite element modelling of a two-dimensional continuum proved to be significantly more straightforward compared to the discrete beam method, which required extensive parametrization and complex grid generation. Notably, the continuum model exhibited superior versatility in mesh generation and geometric adaptability.

When structural configurations demand frequent modifications — such as varying beam distances, inclinations, or transitioning from regular to highly irregular geometries — the continuum approach provides unparallelled flexibility. This adaptability becomes particularly pronounced when structural complexity increases.

From a theoretical perspective, while discrete representations inherently characterize matter at molecular and atomic scales, computational effectiveness necessitates abstraction. When global structural dimensions become significantly larger relative to individual element lengths, the continuum model becomes not only advantageous, but quite indispensable. In the discrete approach, halving inter-beam distances systematically doubles the number of nodes and elements, exponentially increasing computational complexity. Conversely, the continuum model maintains consistent nodal and elemental representations while seamlessly accommodating varied inter-beam relationships within constitutive formulations. These methodological advantages underscore the continuum model's computational efficiency, geometric adaptability, and theoretical elegance in complex structural analysis.

Moreover, in many cases, the continuum formulation allows for the derivation of analytical solutions, which are instrumental in unveiling the structural behaviour of gridshells. This paves the way to a deeper understanding of how geometric and mechanical parameters govern deformation mechanisms and may lead to bifurcation phenomena-insights that would be hardly accessible through purely numerical models.

Experimental validation further corroborated the model's reliability, with experimental data comparison showing a low error margin of approximately 8%. This close alignment between numerical predictions and experimental observations underscores the model's potential for practical engineering applications.

Future research directions will address issues oriented to overcome some limitations of the continuum model. In particular, we recall that its main goal consists in analysing gridshells during the development phase for morphogenetic purposes. In this sense, the model cannot account neither for bracing nor free-edge stiffenings that are usually introduced after deployment. Moreover, the model does not account for eccentricity between the rod registers, in order to obtain a simple analytical formulation.

While the introduction of free-edge stiffening beams could, in general, be done by modelling additional beam elements within the deformed configuration, the introduction of eccentricity and bracing require modifications of the continuum model that are worth of future investigations.

Moreover, alternative formulations, although analogous to the present one, can be investigated in order to replace the Kirchhoff rod description by more accurate ones useful for peculiar materials (e.g. the Timoshenko beam for soft-shear materials).

Complementary to such modelling refinements, it is worth noting that the homogenized shell, while accurate at the macroscopic level, returns cell-averaged member forces and thus cannot reproduce the stress jumps at beam junctions. While such an aspect is not critical in morphogenetic procedures, a standard remedy is a stress-localization post-processing step. Such an enhancement is deferred to future work, to be employed when detailed member-level checks are required.

CRediT authorship contribution statement

Giambattista Romano: Writing – original draft, Software, Methodology, Investigation, Formal analysis, Conceptualization. **Salvatore Sessa:** Writing – original draft, Supervision, Methodology, Investigation, Conceptualization. **Daniele Lancia:** Validation, Data curation. **Luciano Rosati:** Writing – review & editing, Supervision.

Funding and acknowledgements

The present research was carried out under the auspices of the INdAM, Italy - GNFM group, which is gratefully acknowledged by the authors. Research activities has been carried out within the "Modelling, Analysis and DEsign of MOrphing SHElls. MADEMOSHE" project - CUP E53D23003890006 - grant number 2022XFPZ5R - funded by the European Union - Next Generation EU, which is gratefully acknowledged by the authors.

Declaration of competing interest

The authors declare the following financial interests/personal relationships which may be considered as potential competing interests: Salvatore Sessa reports financial support was provided by European Union. If there are other authors, they declare that they have no known competing financial interests or personal relationships that could have appeared to influence the work reported in this paper.

Data availability

No data was used for the research described in the article.

References

[1] Lienhard J, Alpermann H, Gengnagel C, Knippers J. Active bending, a review on structures where bending is used as a self-formation process. Int J Space Struct 2013;28(3–4):187–96.
[2] Bertetto A, Gabriele S, Marmo F, Micheletti A. Shell and spatial structures: Between new developments and historical aspects. Curved Layer Struct 2020;7(1):186–7.
[3] Wang J, Shi D, Zhou C, Zhang Q, Li Z, Marmo F, et al. An active-bending sheltered pathway based on bamboo strips for indoor temporary applications: Design and construction. Eng Struct 2024;307.
[4] Preisinger C. Linking structure and parametric geometry. Archit Des 2013;83(2):110–3.
[5] Goldbach A-K, Bauer AM, Wuchner R, Bletzinger K-U. CAD-integrated parametric lightweight design with isogeometric B-Rep analysis. Front Built Environ 2020;6.
[6] Bauer A, Wüchner R, Bletzinger K-U. Weak coupling of nonlinear isogeometric spatial Bernoulli beams. Comput Methods Appl Mech Engrg 2020;361:112747.
[7] Wright DT. Membrane forces and buckling in reticulated shells. J Struct Div 1965;91(1):173–201.
[8] Yu T, Marmo F, Cesarano P, Adriaenssens S. Continuous modeling of creased annuli with tunable bistable and looping behaviors. Proc Natl Acad Sci USA 2023;120(4).
[9] Gioncu V. Buckling of reticulated shells: State-of-the-art. Int J Space Struct 1995;10(1):1–46.
[10] Pone S, Colabella S, Parenti B, Lancia D, Fiore A, D'Amico B, et al. Construction and form-finding of a post-formed timber grid-shell. In: Structures and architecture: New concepts, applications and challenges. 2013, p. 245–52.
[11] Pone S, Lancia D, Rando D. Reciprocal implications between design and construction process of timber gridshell. Lect Notes Civ Eng 2019;24:251–64.
[12] Fedele R, Placidi L, Fabbrocino F. A review of inverse problems for generalized elastic media: Formulations, experiments, synthesis. Contin Mech Thermodyn 2024;36(6):1413–53.
[13] Kollar L, Hegedus I. Analysis and design of space frames by the continuum method, chemical engineering monographs. Elsevier; 1985.
[14] Wohlever J, Healey T. A group theoretic approach to the global bifurcation analysis of an axially compressed cylindrical shell. Comput Methods Appl Mech Engrg 1995;122(3–4):315–49.
[15] Bruno L, Gabriele S, Grande E, Imbimbo M, Laccone F, Marmo F, et al. Exploring new frontiers in gridshell design: The FreeGrid benchmark. Structures 2023;58.
[16] Buchert K. Buckling of doubly curved orthotropic shells. University of Missouri, Engineering Experiment Station; 1965.
[17] Mateescu D, Gioncu V, Konrad C. Stability of symmetrical load latticed cylindrical roofs. In: The 3rd int. coll. on stability. Timisoara; 1982.
[18] Regalo ML, Gabriele S, Salerno G, Varano V. Numerical methods for post-formed timber gridshells: Simulation of the forming process and assessment of r-funicularity. Eng Struct 2020;206:110119.
[19] Regalo M, Gabriele S, Salerno G, Varano V. A new equivalent continuum model for gridshells. In: IASS symposium 2019-60th anniversary symposium of the international association for shell and spatial structures; structural membranes 2019-9th international conference on textile composites and inflatable structures, FORM and FORCE. 2019, p. 712–9.
[20] Regalo M, Gabriele S, Varano V, Salerno G. Equivalent shell model of elastic gridshells including the effect of the geometric curvature. Appl Mech 2021;2(3):630–49.
[21] Lamacchia E, Pirrera A, Chenchiah I, Weaver P. Morphing shell structures: A generalised modelling approach. Compos Struct 2015;131:1017–27.
[22] Pezzulla M, Stoop N, Jiang X, Holmes DP. Curvature-driven morphing of non-Euclidean shells. Proc R Soc A: Math Phys Eng Sci 2017;473(2201):20170087.
[23] Winslow P, Pellegrino S, Sharma SB. Mapping two-way grids onto free-form surfaces. J Int Assoc Shell Spat Struct 2008;49(158):123–30.
[24] Winslow P, Pellegrino S, Sharma S. Multi-objective optimization of free-form grid structures. Struct Multidiscip Optim 2010;40(1–6):257–69.
[25] Sab K, Lebée A. Homogenization of heterogeneous thin and thick plates. John Wiley & Sons; 2015.
[26] Lebée A, Sab K. Homogenization of a space frame as a thick plate: Application of the bending-gradient theory to a beam lattice. Comput Struct 2013;127:88–101.
[27] Barchiesi E, Placidi L. A review on models for the 3D statics and 2D dynamics of pantographic fabrics. Adv Struct Mater 2017;59:239–58.
[28] Giorgio I, Rizzi N, Turco E. Continuum modelling of pantographic sheets for out-of-plane bifurcation and vibrational analysis. Proc R Soc A: Math Phys Eng Sci 2017;473(2207).
[29] Maurin F, Greco F, Desmet W. Isogeometric analysis for nonlinear planar pantographic lattice: Discrete and continuum models. Contin Mech Thermodyn 2019;31(4):1051–64.
[30] COMSOL multiphysics® v. 5.2, www.comsol.com, COMSOL AB, Stockholm, Sweden.
[31] MSC Software. Theory and user information, vol. A. 2020.
[32] D'Amico B, Kermani A, Zhang H, Pugnale A, Colabella S, Pone S. Timber gridshells: Numerical simulation, design and construction of a full scale structure. Structures 2015;3:227–35.
[33] Schober H. Gridshells: Design, formfinding, construction. Berlin: Ernst & Sohn; 2005.
[34] Brunet Y, Sab K. Mechanical behavior of Chebychev nets. Int J Solids Struct 1989;25(3):251–63.

[35] Gengnagel C, Kilian A, Nembrini J, Scheurer F. Rethinking prototyping: Proceedings of the design modelling symposium berlin 2013. Berlin, Heidelberg: Springer; 2013.
[36] Antman SS. Nonlinear problems of elasticity. Springer; 2005.
[37] Baverel O, Tayeb F, Lefevre B, Caron J-F, du Peloux L. Design and realisation of composite gridshell structures. J Int Assoc Shell Spat Struct 2015;56:49–59.
[38] Colabella S, Lancia D, Repola L, Memmolo R, Pone S. A monitoring system for wooden post-formed gridshells. In: Proceedings of the international association for shell and spatial structures. IASS, Amsterdam; 2015.